



Sulfur isotope and trace element compositions of pyrite determined by NanoSIMS and LA-ICP-MS: new constraints on the genesis of the Shuiyindong Carlin-like gold deposit in SW China

Jin-xiang Li^{1,2} · Rui-zhong Hu^{1,2} · Cheng-hai Zhao¹ · Jing-jing Zhu¹ · Yong Huang^{1,2} · Wei Gao^{1,2} · Jin-wei Li^{1,2} · Yu-zhou Zhuo^{1,2}

Received: 28 September 2018 / Accepted: 1 October 2019
© Springer-Verlag GmbH Germany, part of Springer Nature 2019

Abstract

The Shuiyindong Carlin-like gold deposit, the largest one of this type in China, is located in the Late Paleozoic–Early Mesozoic Youjiang basin. The pyrites in the studied ore bodies (No. I to V) can be divided into four main types plus several sub-types: (1) As-poor pyrites include Py1 (Py1a and Py1b), Py2, and Py3; and (2) As-rich pyrite Py4 (Py4a and Py4b). In situ LA-ICP-MS analyses show that the As-rich pyrite also contains higher Au, Cu, Sb, and Tl than the other pyrite types. In situ NanoSIMS analyses show the $\delta^{34}\text{S}$ variation of Py1 (48.1–67.5‰), Py2 (2.4–7.6‰), Py3 (9.2–14.2‰), and Py4 (–3.0–6.6‰), with the average values of 58.1‰, 5.1‰, 11.4‰, and 3.1‰, respectively. The large $\delta^{34}\text{S}$ variations of As-poor pyrites may reflect a sedimentary source. However, the narrow ranges of $\delta^{34}\text{S}$ values for the As-rich pyrite (Py4) may not reflect a sedimentary but a magmatic or metamorphic origin. A metamorphic sulfur source of Py4 is favored due to paucity of coeval magmatism in the region and decreasing variations of $\delta^{34}\text{S}$ values from Py1 to Py4. Integrated transmission electron microscope (TEM) and NanoSIMS element mapping show that the distribution and concentration of Au are discordant with As and Cu at the submicron scale, also implied by the occurrence of some of Au as nano-submicron particles in Py4. Overall, our new data indicate that the ore fluids were not only enriched in Au but also in As, Cu, and S. Taking an alternative of fluid oxidation probably resulting in the decreasing $\delta^{34}\text{S}$ values of Py4, our result of I to V orebodies indicates the mixing between the underlying metamorphic fluid and meteoric water. Integrated variations in $\delta^{34}\text{S}$ and As–Au–Cu correlations across individual pyrite grains infer the physicochemical changes of aqueous and/or aqueous-carbonic fluids along migration paths.

Keywords Shuiyindong Carlin-like gold deposit · Pyrite · NanoSIMS and LA-ICP-MS analyses · Sulfur isotopes · Trace element compositions

Editorial handling: S.-Y. Jiang

Electronic supplementary material The online version of this article (<https://doi.org/10.1007/s00126-019-00929-w>) contains supplementary material, which is available to authorized users.

✉ Rui-zhong Hu
huruihong@vip.gyig.ac.cn

¹ State Key Laboratory of Ore Deposit Geochemistry, Institute of Geochemistry, Chinese Academy of Sciences, Guiyang 550081, China

² College of Earth and Planetary Sciences, University of Chinese Academy of Sciences, Beijing 100049, China

Introduction

As a significant type of gold deposits worldwide, Carlin-like gold deposit (CLGD) is best known in northern Nevada, the USA, and southwestern China (Arehart 1996; Hofstra and Cline 2000; Hu et al. 2002, 2017a, b; Su et al. 2009a, b, 2018 and references therein). The CLGDs in China and Nevada have many similarities and differences in mineral assemblages, tectonic settings, geologic processes, alteration types, paragenetic sequences, and physical-chemical conditions of mineralization (Ashley et al. 1991; Zhang 1998; Hu et al. 2002; Hofstra et al. 2005; Peters et al. 2007; Su et al. 2009a, 2018; Cline et al. 2013). In southwestern China, the CLGDs are mainly distributed in a “Golden Triangle” in the junction of Yunnan–Guizhou–Guangxi provinces (Fig. 1). Most of the large ones are present in the Guizhou Province, such as the Shuiyindong and Lannigou gold deposits (Zhang et al. 2003; Xiao 2012; Cline et al. 2013; Chen et al.

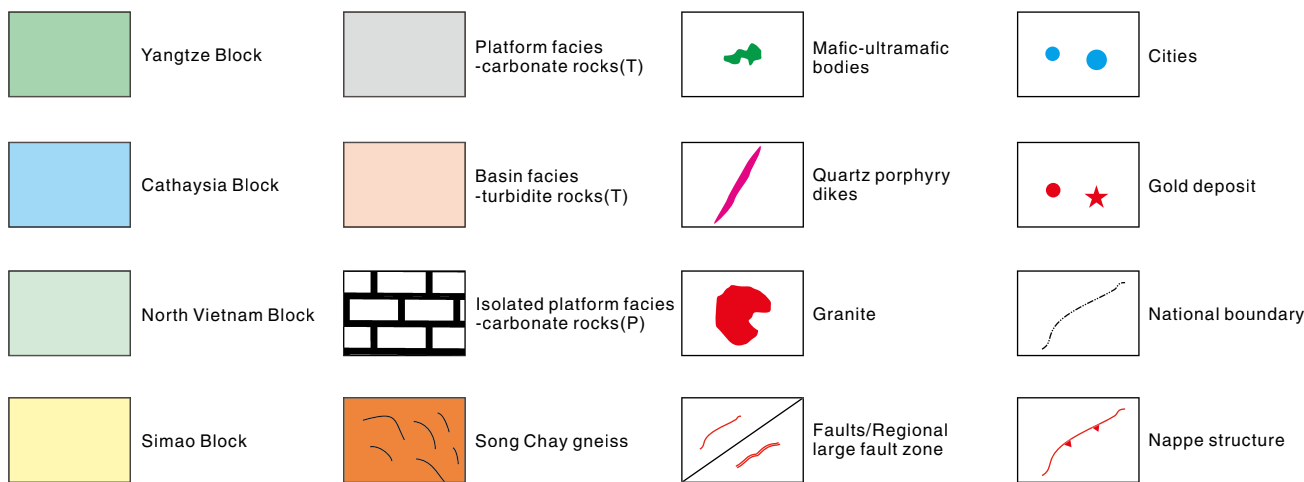
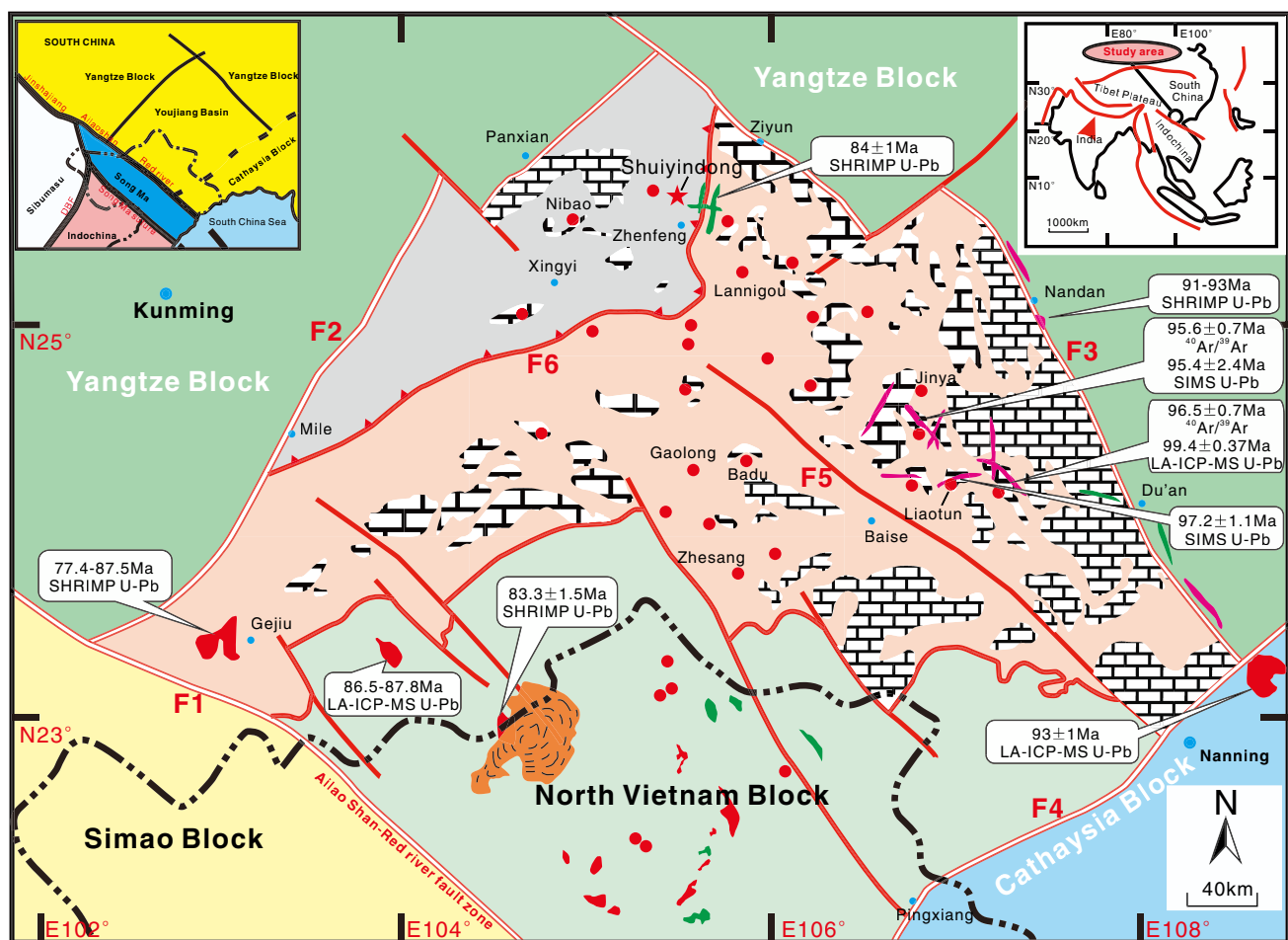


Fig. 1 Simplified geologic map showing the distribution of sediment-hosted disseminated Au deposits in the Youjiang basin (modified from Chen et al. 2012, 2015b; Hou et al. 2016; Nevolko et al. 2017). F1:

Honghe Fault; F2: Panxian-shizong Fault; F3: Ziyun-du'an Fault; F4: Pingxiang Fault; F5: Youjiang Fault; F6: Poping Nappe Structure

2015a, b; Hu et al. 2017a), hosted in Late Paleozoic and Early Mesozoic sedimentary rocks in the southwestern margin of the Yangtze craton (Su et al. 2009b). Based on ore geometry, host lithology, and controlled structure, some researchers have further divided the CLGDs in this region into strata-bound type, such as the Shuiyindong gold deposit, and fault-bound type controlled by

high-angle reverse faults, such as the Lannigou gold deposit (Fig. 1; Liu and Liu 2005; Guo and Zhou 2006; Chen et al. 2015b; Tan et al. 2015a, 2017). CLGDs in this region share similar wall-rock alterations to the classic CLGDs in Nevada, such as decarbonatization, silicification, argillization, carbonatization, sulfidation, or pyritization (Hofstra and Cline 2000; Cline et al.

2005). They are generally low temperature ($< \sim 250$ °C), low to moderate salinity (< 6 wt% NaCl equiv), low to moderate CO_2 abundance, rich in H_2S , and relatively reduced condition for the ore-forming fluids (Hu et al. 2002).

Many attempts have been made to determine the mineralization age of CLGDs in this region (Fig. 1). For example, the sericite in the quartz veins of the Lannigou gold deposit yielded a $^{40}\text{Ar}/^{39}\text{Ar}$ plateau age of 194.6 ± 2 Ma (Chen et al. 2009a). The hydrothermal rutile and sericite from the Zhesang gold deposit in the region yielded the $^{40}\text{Ar}/^{39}\text{Ar}$ and SIMS U-Pb ages of 215.3 ± 1.9 Ma and 213.6 ± 5.4 Ma, respectively (Pi et al. 2016, 2017). The hydrothermal apatite from the Nibao gold deposit yielded the SIMS Th-Pb age of 141 ± 3 Ma (Chen et al. 2019). The hydrothermal calcite from the Zimudang gold deposit yielded the Sm-Nd age of 148 ± 5 Ma (Wang 2013). Based on the relatively reliable ages, there might be two episodes of gold mineralization in the region, one about 200–230 Ma in the southern basin and another about 130–150 Ma in the northern basin, corresponding to Indosinian and Yanshanian orogeny (Hu et al. 2017a; Su et al. 2018).

The age, geology, and style of mineralization of the Shuiyindong gold deposit have been well studied in the last two decades (Zhang et al. 2003, 2005; Xia 2005; Liu et al. 2006a; Su et al. 2008, 2009a, b, 2012, 2018; Xiao 2012; Wang et al. 2014; Hou et al. 2016). And two groups of ages were given by a pyrite/arsenopyrite Re-Os isochron age of 235 ± 33 Ma (Chen et al. 2015a) and calcite Sm-Nd isochron ages from 134 ± 3 Ma to 136 ± 3 Ma (Su et al. 2009a), respectively. However, Chen et al. (2019) themselves pointed out that the age of 235 ± 33 Ma could be problematic and eliminated because the samples have been mixed by multiple generations of sulfides and have low Re and Os contents. According to the field observation and nearby the Shuiyindong mining district, there is a remnant exposure of Jurassic sedimentary rocks (~ 0.7 km²) that were conformable to and folded together with the Late Triassic rocks (Wang 1997; Su et al. 2018), suggesting a maximum limit of Jurassic age for the Shuiyindong deposit. These facts indicate that the mineralization of the Shuiyindong gold deposit is more likely to be consistent with the second episode of gold mineralization in the region.

The Yanshanian (ca. 140 Ma) and Indosinian (ca. 215 Ma) granite and granite-related W-Sn polymetallic deposits have been recognized in the southern and eastern parts of the Youjiang basin (Hu et al. 2017b), whereas they are rare inside the basin. Indosinian (Triassic) magmatism produced voluminous granitic plutons in South China, particularly in Hunan, Jiangxi, and Guangxi Provinces (Hu and Zhou 2012). Although there is no Indosinian granite exposed in the Youjiang basin, there occur a few Indosinian W-Sn deposits (e.g., Xinzhai and Nanyangtian; Feng et al. 2011). It is reasonable to infer Indosinian hidden granite intrusions in this region.

The sources of the ore-forming metals and fluids have been investigated using stable isotopes, such as S isotopes of

sulfides (Zhang et al. 2010; Wang et al. 2013; Tan et al. 2015b; Hou et al. 2016), H-O isotopes of fluid inclusions in quartz (Hu et al. 2002; Wang 2013; Peng et al. 2014; Tan et al. 2015b), and C-O isotopes of calcite (Su et al. 2009a; Zhang et al. 2010; Tan et al. 2015b, 2017). Although many efforts have been made by previous scholars, uncertainties remain regarding the ore-forming mechanism and genetic model, probably due to the lack of high-quality geochemical data.

Taking sulfur isotopes and geochemical compositions of pyrite as an example, it is well known that the gold-bearing minerals in the CLGDs are dominantly very fine zoned pyrite grains (Hofstra and Cline 2000; Hu et al. 2002; Cline et al. 2005; Su et al. 2008). Therefore, the previous analyses using pyrite separates are less convinced to distinguish the sulfur isotopes and trace element compositions between pre-ore stage and ore-stage pyrites. For that reason, Hou et al. (2016) have attempted to determine sulfur isotope and trace elemental compositions of pyrite using sensitive high-resolution ion microprobe (SHRIMP) and laser ablation-inductively couple plasma-mass spectrometry (LA-ICP-MS), respectively. In this study, we utilized high-resolution in situ NanoSIMS (nano secondary ion micro-spectrometry) technique, which offers much higher spatial resolution down to nanometer scale (~ 100 nm) and much smaller spot size ($2 \mu\text{m}$) to validate the $\delta^{34}\text{S}$ variations and trace element distributions across individual pyrite crystals. By using NanoSIMS, we identified a pyrite type with superheavy sulfur isotopic compositions. Furthermore, apart from in situ LA-ICP-MS technique, we combined TEM methods to identify the occurrence of nano-submicron Au particles. On the basis of these analyses, we try to decipher the origin and evolution of sulfur for the Shuiyindong gold deposit.

Geological background

The Yunnan-Guizhou-Guangxi contiguous region (also named as Dian-Qian-Gui region) is commonly referred to as the “Golden Triangle”, with many major CLGDs present in the Youjiang basin in this region (Fig. 1; Chen et al. 2015b). Tectonically, the Youjiang basin is located in the southwestern margin of the Yangtze craton. It is bounded to the southwest by the Red river fault (F1), the northwest by the Shizong-Mile fault (F2), the northeast by the Ziyun-Du’an fault (F3), and the southeast by the Pingxiang-Nanning fault (F4). The Youjiang basin was developed on the Late Paleo- to Neoproterozoic basement and has experienced at least three phases of evolution: a rift basin on a passive continental margin from the Early Devonian to Early Permian, a back-arc rift basin from the Late Permian to Middle Triassic, and a foreland basin in the Late Triassic (Liu et al. 2002; Hu et al. 2017a), corresponding to the opening, subduction, and closure of Paleo-Tethys Ocean, respectively (Du et al. 2013; Chen et al. 2015a). Lithologically, the basin consists of Late Paleo- to Neoproterozoic low-grade

metamorphic rocks and overlying thick shale and carbonate sequences of Cambrian to Triassic age (Hu et al. 2002, 2017a; Peters et al. 2007; Su et al. 2008; Hu and Zhou 2012). Granite plutons with ages varying from Triassic (Indosinian) to Jurassic-Cretaceous (Yanshanian) are present at the margins, the east and south of the basin (Hu and Zhou 2012; Mao et al. 2013; Pi et al. 2017; Zhu et al. 2017; Yan et al. 2018).

The exposed strata in the basin can be further divided into two parts, Permian-Triassic platform facies strata (located to the northwest of F6; Fig. 1) composed of thin layers of carbonates, siliceous rock, mudstone and pyroclastics, and Middle Triassic basin facies strata (located to the southeast of F6; Fig. 1) composed of terrigenous detrital turbidite, such as calcareous sandstone, siltstone, and mudstone (Fig. 1; Suo et al. 1993; Chen et al. 2015b).

Ore deposit geology

The Shuiyindong gold deposit is one of the largest CLGDs in China, including four ore blocks such as Shuiyindong, Xionghuangyan, Bojitian, and Nayang from west to east (Fig. 2). It is situated in the eastern limb of the E-W-trending Huijiabao anticline, approximately 20 km northwest of the Zhenfeng county in SW Guizhou province. The total proven gold reserve for the deposit (Fig. 2) is 265 metric tonnes (ca. 8.515 Moz), with an average grade of 5 g/t (Su et al. 2018). Generally, the boundaries between orebodies and wall rocks are gradational and can only be defined by cut-off grade (1 g/t). The sedimentary rocks in the Shuiyindong gold deposit include Middle-Upper Permian and Lower Triassic bioclastic limestone, siltstone, and argillite, such as massive bioclastic limestone of the Middle Permian Maokou Formation (P₂m) overlaid by the Upper Permian Longtan (P₃l), Changxing (P₃c), and Dalong (P₃d) formations, and the Lower Triassic Yelang Formation (T₁y) and Yongningzhen Formation (T₁yn) (Fig. 2).

Gold mineralization mainly occurs in the center of the eastern part of the Huijiabao anticline, associated with the bioclastic limestone and calcareous siltstone of the first and second unit of the Longtan Formation (P₃l¹ and P₃l²) (Fig. 3; Liu 2001; Su et al. 2009b; Tan et al. 2015b). The first unit mainly consists of argillite and the second unit mainly consists of silty argillite with bioclastic limestone or coal streaks interlayers. Tan et al. (2015a) reported that the different host rocks were preferentially mineralized by different elements. The bioclastic limestone is relatively more enriched in Au, whereas the argillite is more enriched in As, Hg, Sb, and Tl, and the unconformity contact between P₂m and P₃l and the axis of the anticline might be the pathways of the ore-forming fluids. It is worth to note that no coeval igneous rocks have been recognized in the mining area.

Alterations and mineral paragenesis

In the Shuiyindong gold deposit, a single orebody (zone) as defined by Au cut-off grade is commonly narrower than the associated pyrite-mineralized zone (Fig. 4a). The most important alteration types in the mineralized zones are decarbonatization, silicic alteration, sulfide alteration, and argillization (Fig. 4a–h, j and ESM Fig. 1b, f, k, l; Cline et al. 2013; Hou et al. 2016). Carbonate minerals have been intensely dissolved in many rocks and locally cemented by quartz and illite (ESM Fig. 1k, l), which has enhanced porosity of ore rocks and facilitated the occurrence of high-grade ores within collapsed breccias (Fig. 4e, Hou et al. 2016). Silicic alteration occurred widely as disseminated quartz or veinlets, especially at the unconformity contact between P₂m and P₃l (Fig. 4e–g, k, l). Argillization mainly included potassium-aluminum silicate mineral assemblages of illite (± kaolinite) (Fig. 4f, l). Sulfide alteration presented as various sulfides including pyrite, arsenopyrite, realgar (± orpiment), along with minor stibnite and sphalerite (Figs. 4b, c, f, j–l and 5a–l). Au-bearing pyrite concentrated in the deformed and brecciated areas (Fig. 4e), surrounded by disseminated jasperoid quartz with illite, ferroan calcite, or ankerite (Fig. 4k, l and ESM Fig. 1k, l), and host rock can be cut by late calcite veins in some places (Fig. 4i). Based on microscopic textural observations, four types of pyrite have been recognized. They are described below, in the order of formation from Py1 to Py4.

Py1 is present in most samples. It is considered to be the earliest pyrite in the samples (Hou et al. 2016). It can be subdivided into two sub-types, framboidal clusters (Py1a, ESM Fig. 1a) surrounded by euhedral, commonly isolated crystals (Py1b, ESM Fig. 1e, l). The Py1a framboidal is extremely fine-grained (0.1–4 μm) and is thought to be synsedimentary or early diagenetic origin (Liu et al. 2006b; Hou et al. 2016), whereas the clusters are commonly associated with pore spaces and surrounded by quartz, dolomite, and illite. Py1b is much larger, with diameter between 25 and 200 μm, mostly > 50 μm. This type of pyrite is most common in the P₃l² sedimentary rocks such as argillite and bioclastic limestone.

Py2 is subhedral-anhedral grain with a porous spongy texture, with grain size from 10 to 100 μm in diameter (ESM Fig. 1a–d, f, g, i–k). The spongy feature is probably due to diagenetic origin or inversion of marcasite to pyrite, which involves an increase in density and therefore decrease in volume (Murowchick 1992; Su et al. 2008). It commonly occurs as disseminated grains in calcareous siltstones with abundant organic matters (ESM Fig. 1f) or aggregates (nodules) in impure bioclastic carbonates (ESM Fig. 1j, k). Most Py2 grains have large overgrowths of Py3 (ESM Fig. 1b–d, g, j, k) or Py4 (ESM Fig. 1a, i).

Py3 is generally homogenous under microscope. It is subhedral to euhedral, with grain size varying from 20 to 200 μm in diameter (ESM Fig. 1b–g, j, k). Some grains contain small sphalerite inclusions (Sp1; ESM Fig. 1g and ESM

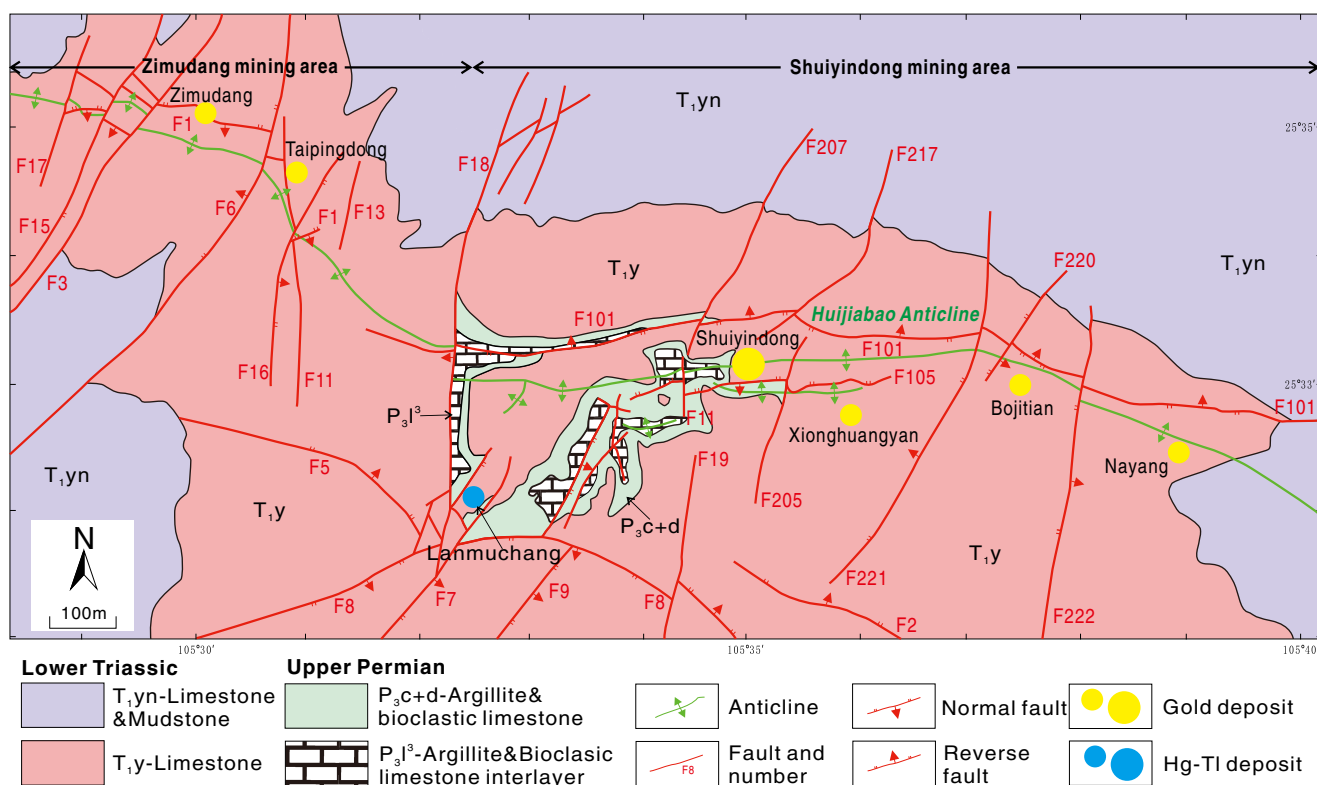


Fig. 2 Structural map of the study area, showing the major structural faults and the locations of the gold deposits (modified from Hou et al. 2016; Tan et al. 2017)

Fig. 2b). Py3 commonly overgrew on the deformed or corroded surfaces of Py2 (ESM Fig. 1b–d). Some Py3 grains were crosscut by Py4 (ESM Fig. 1h, i).

Py4 is subhedral-euhedral grain with diameter varying from 10 to 200 μm (ESM Fig. 1a–l). Oscillatory compositional zoning (mainly due to As fluctuation) is well developed in Py4 (ESM Fig. 1b, d, i, l). The compositional zonation is more complicated in the deformed grains (ESM Fig. 1b–d). Those fault zones-related are commonly overgrowing on small corroded pyrite cores and are referred to as Py4a (ESM Fig. 1b–d, j). Those undeformed bioclastic limestone associated pyrite are overgrowing on a pentagonal dodecahedral core of (Py1b), and are referred to as Py4b (ESM Fig. 1e). Some native gold nanoparticles have been found to be associated with both Py4a and Py4b (ESM Fig. 2a, b).

Some Py4 grains are surrounded by arsenopyrite aggregates or overgrowths (ESM Fig. 1f, i). During the waning stage of hydrothermal fluid, realgar, orpiment, and stibnite (Fig. 4b, f) are present in late carbonate veins associated with the faults that cut the ore-rich strata. Sphalerite (Sp2) occurs in the microfractures of Py4 (ESM Fig. 1d). The general paragenesis sequence based on the textural observations is listed in Fig. 5. In short, the inferred crystallization sequence is Py1 \rightarrow Py2 \rightarrow Py3 (Sp1) \rightarrow Py4 \rightarrow arsenopyrite \rightarrow realgar, orpiment, and stibnite and Sp2.

Sample descriptions and analytical methods

Sample locations

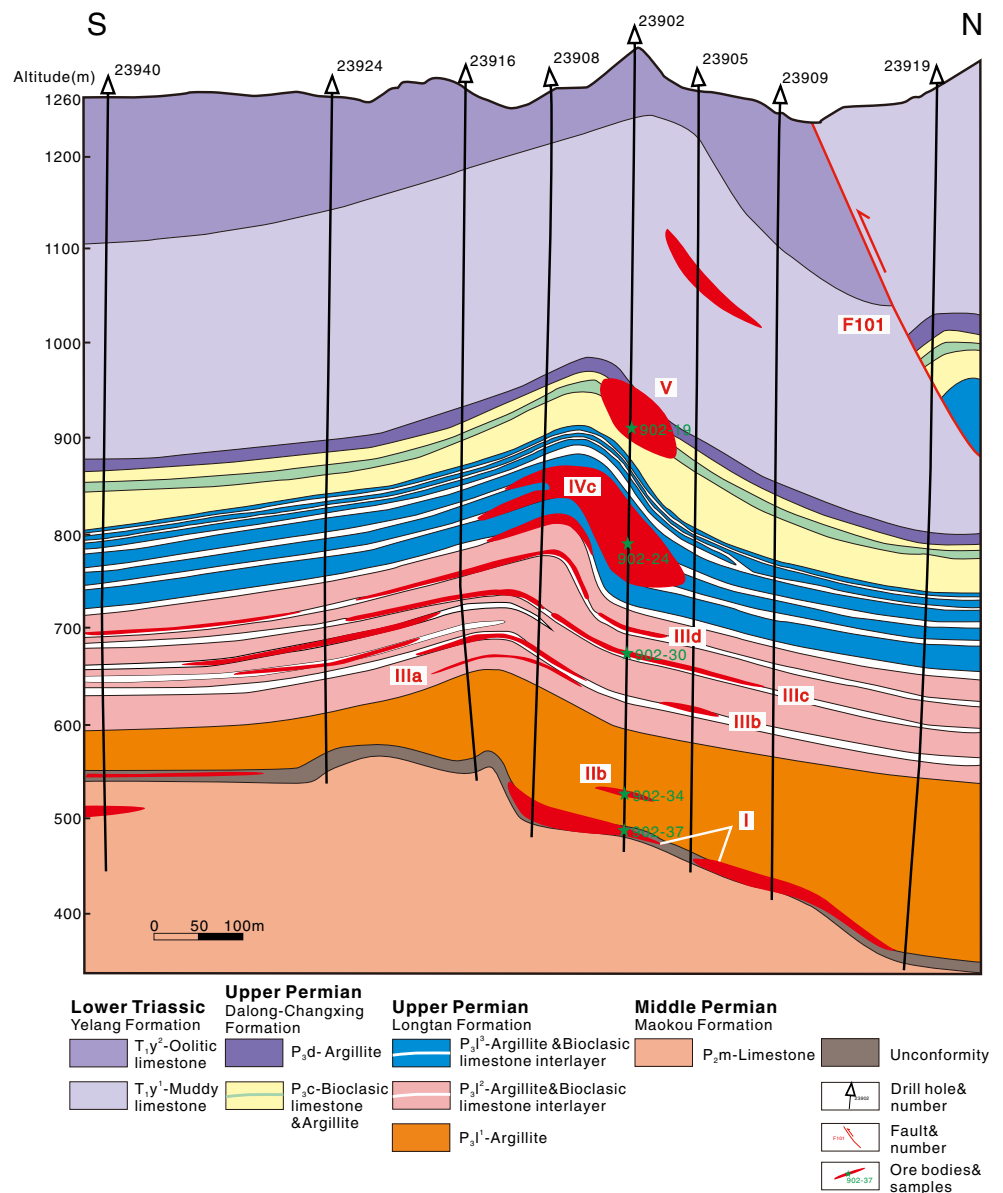
The samples used in this study were collected from underground mining tunnels and a drill core (ZK23902) of the Shuiyindong gold deposit, covering most orebodies from the bottom No. I to the top No. V (Fig. 3). These samples are selected to study the vertical and lateral variations of sulfur isotopes and trace element concentrations of pyrite at the deposit scale. The depths of samples from the drill core and the underground mining tunnels are shown in Fig. 3. Information about Au grade, lithology, and detailed locations are listed in ESM Table 1.

Analytical methods

AAS tests and SEM-EPMA analysis

The Au grades of the rock samples used in this study (ESM Table 1) were determined in analytical laboratory of the ALS Chemex Ltd. in Guangzhou, China. The atomic absorption spectroscopy (AAS) and the gravimetric methods were used for low (< 10 ppm) and high (> 10 ppm) concentrations, respectively. Back-scattered electron (BSE) and secondary

Fig. 3 Simplified locations of analyzed samples of ZK23902 drill hole (after Tan et al. 2017)



electron images of the polished thin sections of the samples were acquired using a JEOL JSM7800F SEM under the operation conditions of 10–15 kV, 10 nA, and a beam size of 1 μm in diameter at the State Key Laboratory of Ore Deposit Geochemistry, Chinese Academy of Sciences, Guiyang, China. The concentrations of major and minor elements in pyrite and arsenopyrite in the samples were determined using a JEOL JXA-8230 EPMA under the operation conditions of 15 kV, 10 nA, and a beam size of 1 μm in diameter, count time 10 s (peak) and 5 s (backgrounds) in the Analytical Center of the Shandong Bureau of Metallurgy and Geology of China. The characteristic x-rays used are Fe ($K\alpha$), S ($K\alpha$), As ($L\alpha$), Au ($L\alpha$), Ni ($K\alpha$), Co ($K\alpha$), Cu ($K\alpha$), and Se ($L\alpha$). The standard materials for each element are as follows: pyrite (FeS_2) for Fe and S, arsenopyrite (FeAsS) for As, pentlandite

($(\text{Fe,Ni})_9\text{S}_8$) for Ni, galena (PbS) for Pb, gold (Au^0) for Au, skutterudite ($[(\text{Co, Ni, Fe})\text{As}_{3-x}]$) for Co, (silver) Ag^0 for Ag, cuprite (Cu_2O) for Cu, stibnite (Sb_2S_3) for Sb, bismuth selenide (Bi_2Se_3) for Se, and sphalerite (ZnS) for Zn, respectively. The analytical errors are < 1% for Fe and S, and < 10% for As, Ni, Pb, Au, Co, Ag, Cu, Sb, Se, and Zn. The matrix effects were corrected using the in-house ZAF software.

In situ NanoSIMS/SHRIMP and bulk sulfur isotope analysis of pyrite

In situ S isotope analysis and element/isotope mapping (both line and plane scans) were carried out using a CAMECA NanoSIMS 50L instrument at the Institute of Geology and Geophysics, Chinese Academy of Sciences,

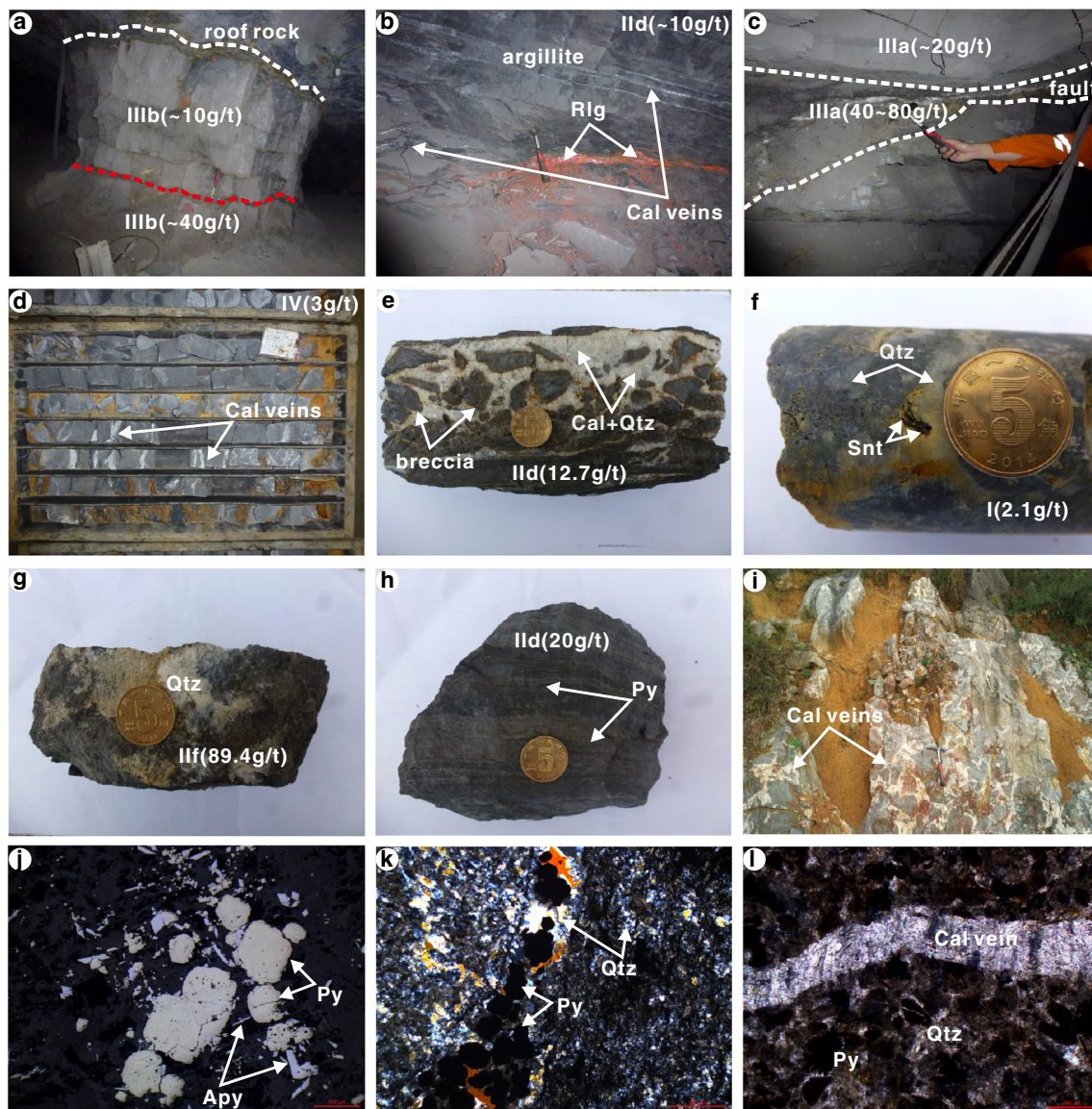


Fig. 4 Photographs of mining pit, drill cores, and hand specimens, showing the alteration, mineralization, and ore textures of the Shuiyindong gold deposit: **a** Bioclastic limestone of IIIb orebody showing the clear boundaries of ore rock and roof rock (marked as the white dotted line), high Au grade and low Au grade of ore rocks (marked as the red dotted line). **b** Extensive bedding realgar-calcite veinlets of IId orebody. **c** Fine grained disseminated pyrite near the fault zones. **d** Extensively occurrence of calcite veinlets from ZK23902 drill cores. **e** Strongly silicified breccia from high deformation zone showing a relatively high Au grade. **f** Stibnite-hosted silicified ore rock from ZK23902

drill cores. **g** Bioclastic limestone showing sulfide and silicification. **h** Fine-grained disseminated texture of argillite showing extensive sulfidation. **i** Ore-unrelated calcite veins, located outside of the Shuiyindong mining area. **j** Reflected light photomicrograph of arsenian pyrite, overgrown by arsenopyrite. **k** Transmitted light photomicrograph of arsenian pyrite concentrated along the quartz vein and jasperoid quartz. **l** Transmitted light photomicrograph of arsenian pyrite and jasperoid realgar, crossed by late calcite veinlet. *Apy* arsenopyrite, *Py* pyrite, *Rlg* realgar, *Snt* stibnite, *Cal* calcite, *Qtz* quartz

Beijing, China. The methodology is described in detail by Zhang et al. (2014b). Below is a brief description. A primary Cs^+ ion beam of 1–2 pA and 100 nm in diameter was used for both types of analysis. ^{32}S was counted by Faraday cup (FC) to avoid the quasi-simultaneous arrival (QSA) effect, and ^{34}S and other elements were counted with electronic multipliers (EMs) (Yan et al. 2018). The standard-sample-standard bracketing method was applied to correct for instrumental mass fractionation. Certified

international standards (including Pyrite of Balmat, CAR-123 pyrite) and internal reference samples (pyrite PY-1117 and CS01) were used during S isotope analysis. The beam size was 2 μm in diameter. The analytical precision (1σ) was about ± 0.5 per mil. Mapping areas range from 25×25 to $50 \times 50 \mu\text{m}$ and the corresponding resolution is 256×256 or 512×512 pixels. Necessarily to point out, the numerical color scales of the obtained images indicate relative signal intensities, and do not

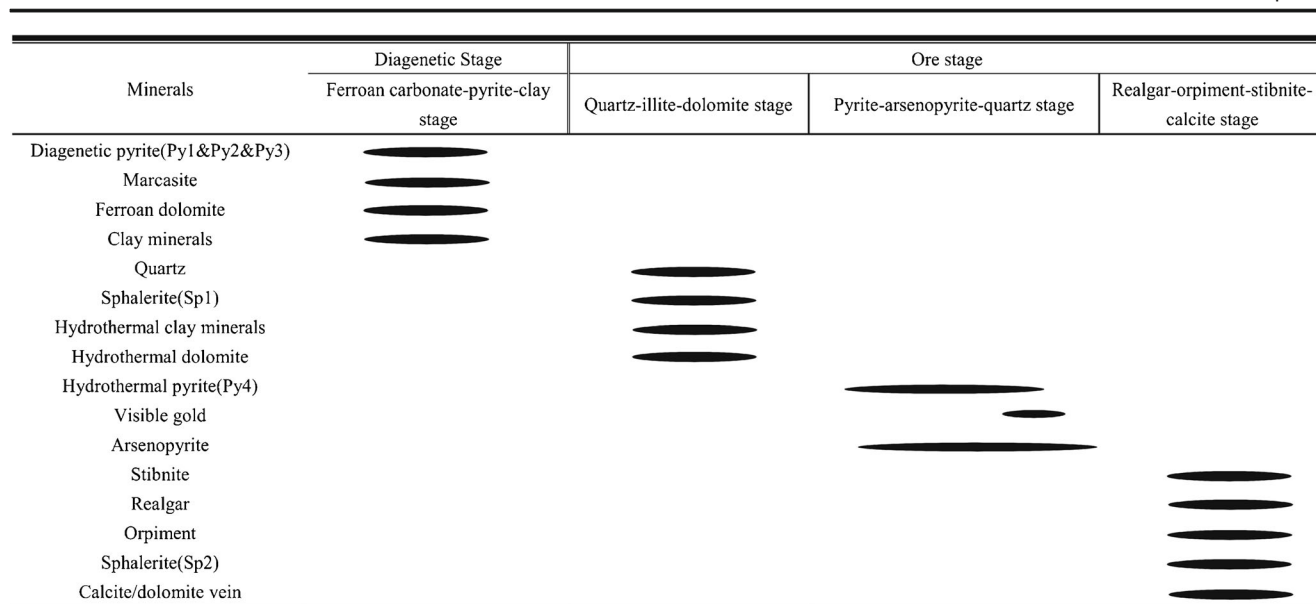


Fig. 5 Paragenetic sequence of the Shuiyindong gold deposit, showing the generalized alteration and mineral paragenesis

represent actual concentrations of the analyzed elements, hence, different images are not comparable in the scales of signal intensities (Yan et al. 2018). In situ S isotope analyses for some pyrite grains were performed by SHRIMP SI at the Australian National University (ANU), Canberra, Australia. The spot size was 10 μm . The results were normalized to the Ruttan pyrite standard, and the internal precision for unknowns during the session was between 0.020 and 0.154‰. Analytical techniques are as described by Tanner et al. (2016). Bulk S isotope analyses were carried out using a Finnigan MAT-253 mass spectrometer at the State Key Laboratory of Ore Deposit Geochemistry, Institute of Geochemistry, Chinese Academy Sciences, Guiyang, China. GBW 04415 and GBW 04414 Ag_2S are used as the external standards and the Vienna Canyon Diablo Troilite (V-CDT) as reference standard, with an analytical precision of $\pm 0.2\%$ (2σ).

In situ LA-ICP-MS trace element analysis of pyrite

On the same spots analyzed for S isotopes by NanoSIMS, trace element analysis of pyrite was conducted by LA-ICP-MS at the Sample-Solution Analytical Technology Co., Ltd., Wuhan, China. Detailed operating conditions for the laser ablation system and the ICP-MS instrument, and data reduction are the same as described by Zong et al. (2017). Laser sampling was performed using a GeolasPro laser ablation system that consists of a COMPexPro 102 ArF excimer laser (wavelength of 193 nm and maximum energy of 200 mJ) and a MicroLas optical system. An Agilent 7700e ICP-MS instrument was used to acquire ion-signal intensities. Helium was applied as a carrier gas. Argon was

used as the make-up gas and mixed with the carrier gas via a T-connector before entering the ICP. A “wire” signal smoothing device is included in this laser ablation system (Hu et al. 2015). The spot size and frequency of the laser were set at 24 μm and 5 Hz, respectively for this study. Trace element compositions of pyrite were calibrated against various reference materials (MASS-1 and NIST 610) and then quantified against the MASS-1 synthetic pyrite and NIST 610 standards using Fe as the internal standard. Each analysis incorporated a background acquisition of approximately 20–30 s followed by 50 s of data acquisition from the sample. Analytical processes are as described by Large et al. (2007). An Excel-based software ICPMSDataCal was used to perform off-line selection and integration of background and analyzed signals, time-drift correction, and quantitative calibration for trace element analysis (Liu et al. 2008). The analytical results of the references are in agreement with the recommended values.

FIB-TEM analysis

Focused ion beam scanning electron microscope (FIB-SEM) preparing samples for transmission electron microscope (TEM) analysis was performed using an FEI Scios Dual beam at the Center for Lunar and Planetary Sciences, Institute of Geochemistry, Chinese Academy of Sciences, Guiyang, China. The FEI Scios Dual Beam combines a traditional field emission electron column with an FIB column and equipped with energy-dispersive X-ray spectroscopy (EDS) and electron backscattered diffraction (EBSD) detectors. Ultra-thin slices were examined by a field emission transmission electron microscope (Tecnai G2 F20 S-TWIN, FEI Inc., USA) equipped with an energy dispersive

spectrometer, in the State Key Laboratory of Environmental Geochemistry, Institute of Geochemistry, Chinese Academy of Sciences, Guiyang, China. The techniques employed included the high magnification bright field topography imaging analysis, high-resolution lattice imaging analysis, selected area electron diffraction (SAED) analysis, and Fourier transform structural analysis.

Results

Major elements in pyrite

The compositions of pyrites acquired by EPMA from the deposit are listed in ESM Table 2. And the whole dataset is tabulated in ESM Table 3. The contents of As are < 0.14 wt.% (0.04 wt.% average) in Py1, < 0.34 wt.% (0.05 wt.% average) in Py2, < 1.59 wt.% (0.27 wt.% average) in Py3, and < 9.32 wt.% (3.72 wt.% average) in Py4. The concentration of Au analyzed is below the detection limit (bdl) of EPMA in Py1 and Py2, < 0.03 wt.% in Py3, and < 0.29 wt.% in Py4. The concentrations of Cu are below the detection limits of EPMA in Py1, < 0.06 wt.% in Py2, < 0.07 wt.% in Py3, and < 0.23 wt.% in Py4.

Sulfur isotope compositions of sulfides

The sulfur isotopic compositions of sulfides from the Shuiyindong gold deposit are compiled for comparison in ESM Table 4 and the whole dataset of in situ analyses of pyrites is provided in ESM Table 5. The variations are illustrated in Fig. 6. The most dramatic changes are between the the Au-poor (Py1, Py2 and Py3) and the Au-rich varieties (Py4a/4b). The results for a total of 35 analyses show that Py1a and Py1b have superheavy $\delta^{34}\text{S}_{\text{CDT}}$ values ranging from 63.0 to 67.5‰ (average 65.0‰) and from 48.1 to 67.3‰ (average 57.2‰), respectively. The superheavy and unfrequent values were matched with the results ($n = 5$, 56.9–75.7‰, average 65.6‰) acquired at ANU with SHRIMP SI, which elucidates the existence and repeatability. The $\delta^{34}\text{S}$ values of Py2 (2.4 to 7.6‰, average 5.1‰, $n = 11$) and Py3 (9.2 to 14.2‰, average 11.4‰, $n = 22$) are much lower than those of Py1 but still elevated. The $\delta^{34}\text{S}$ values of Py2 and Py3 are similar to ranges of pyrite formed by biogenic and abiogenic sulfate reduction in the Paleozoic (Fig. 7; Hou et al. 2016). In contrast, the Au-rich varieties Py4a and Py4b have relatively low $\delta^{34}\text{S}$ values, varying from -1.2 to 6.6‰ (average 3.6‰, $n = 97$) and from -3.0 to 5.8‰ (average 2.6‰, $n = 100$), respectively. The $\delta^{34}\text{S}$ values for stibnite ($n = 4$) and realgar ($n = 5$) in this study are from 1.6 to 2.1‰ and from 2.6 to 2.7‰, respectively.

The average $\delta^{34}\text{S}$ values of Py4 from orebodies I at the bottom, through II-III-IV in the middle, to V at the top decrease from 4.1‰ (4.0–4.3‰) \rightarrow 3.7‰ (-1.1~+ 6.1‰) \rightarrow 3.0‰ (0.7~5.8‰) \rightarrow 2.7‰ (-2.0~+ 5.7‰) to 1.3‰ (1.2~1.5‰).

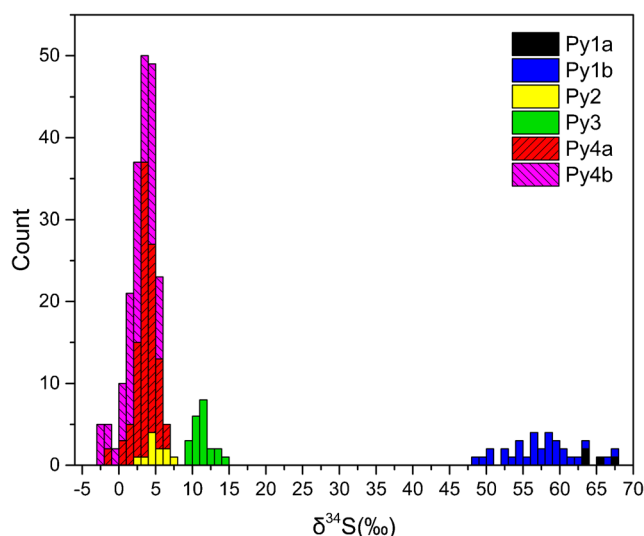


Fig. 6 Histogram of NanoSIMS S isotopic compositions of pyrites, showing the different ranges of $\delta^{34}\text{S}$ values

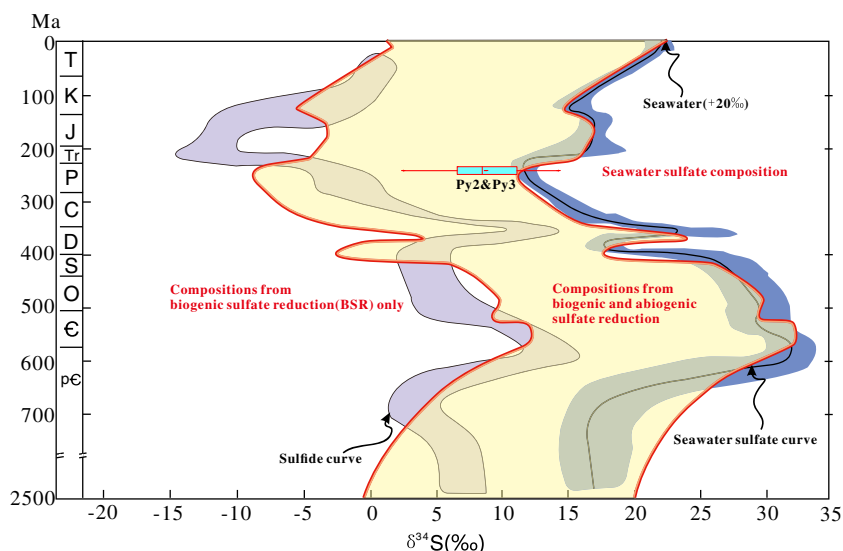
TEM results

SEM images and NanoSIMS mapping shown in the previous description imply the presence of micro-nanoscale particulate Au in arsenian pyrite. In this scenario, to examine this hypothesis and acquire further insight into the mode of Au at the nanoscale, we made detailed TEM observation of five FIB thin sections from the high-grade ore rocks. The results show increasing As contents from Py1b to Py3 and to outermost Py4 (Fig. 8a–c), consistent with the results from LA-ICP-MS and NanoSIMS analyses. Furthermore, the HRTEM image reveals the occurrence of five Au nanoparticles (< 10 nm) further detected by EDS throughout the As-rich rim (Fig. 8d, inset). The matrix surrounding the nanoparticles is randomly oriented arsenian pyrite.

Trace element composition of pyrite

Apart from the Py1a grains being too small to acquire available data, the concentrations of trace elements in Py1b, Py2, Py3, and Py4 from the Shuiyindong gold deposit, determined by LA-ICP-MS, are listed in ESM Table 6. And the raw data of MASS-1 is shown in ESM Table 7. The sample (Z902-24-02, Py4a) containing sphalerite inclusions has unusually high Zn content (48,803 ppm, marked with an asterisk, see ESM Table 6). Figure 9 shows the ranges of selected trace elements for different types of pyrite such as Py1b ($n = 7$), Py2 ($n = 7$), Py3 ($n = 20$), Py4a ($n = 19$), and Py4b ($n = 26$). For comparison, co-variations of some element pairs are illustrated in Fig. 10. Py1b is characterized by a wide range of trace element abundances, with the highest being Se (0–229 ppm) and Mn (0.31–10.95 ppm). Compared to Py1, Py2 has elevated As (35.78–26,949 ppm), V (0.01–0.96 ppm), Co (1.72–325 ppm), Au (0–0.08 ppm), Ni (4.44–1769 ppm), Cu (2.62–516

Fig. 7 Variation of $\delta^{34}\text{S}$ values of Py2&Py3 with the marine sulfate and sulfide curves (blue box represents S isotope area of Py2&Py3, modified from Chang et al. 2008; Hou et al. 2016)



ppm), Ag (0–0.12 ppm), Sb (0.95–42.80 ppm), Tl (0.12–2.98 ppm), and W (0–0.07 ppm), but lower Mn (0–11.06 ppm) and Se (0–190 ppm) abundances. Compared to Py2, Py3 has more variable but roughly higher As (up to 10,984 ppm), Au (up to 0.73 ppm), V (up to 17 ppm), Co (0.02–175 ppm), Ni (up to 253 ppm), Cu (2.96–694 ppm), Sb (0–148 ppm), Tl (0.03–4.45 ppm), Sn (0–16.73 ppm), and W (0–0.45 ppm) but lower Mn (0–1757 ppm) and Se (0–72.63 ppm) abundances. Py4a/4b have the highest As (164–54,955 ppm), Au (up to 538

ppm), V (up to 14.63 ppm), Co (0.31–963 ppm), Ni (0.60–4057 ppm), Cu (8.72–902 ppm), Zn (0–48,803 ppm), Ag (0.02–9.46 ppm), Sb (1.84–285 ppm), Tl (0.10–22.37 ppm), Sn (up to 9.30 ppm), and W (up to 14.36 ppm) but the lowest Mn (<29.77 ppm) and Se (<129 ppm) abundances. In summary, the average values of Au in Py1-3 are 0.01, 0.02, and 0.11 ppm, and those in Py4a and Py4b are 2.65 and 2.26 ppm, respectively. The maximum value of Au increases from 0.08 ppm in Py2, 0.73 ppm in Py3, 79.0 ppm in Py4a, to

Fig. 8 Photographs of FIB-TEM work of the Shuiyindong gold deposit. **a** BSE image of selected sample (the white dashed rectangle responds to the area **b** and the white arrow represents the direction of FIB slice of **c**). **b** Image of micro-scale visible native gold (bright particles marked by white arrows) by SEM. **c** White arrow, yellow dashed line, and white number showing the different layers. **d** TEM image of No.3 layer in (c), circular dashed lines show Au nanoparticles (Nps), with the EDS spectra attached to the top right (the signal of Cu originates from the copper grid)

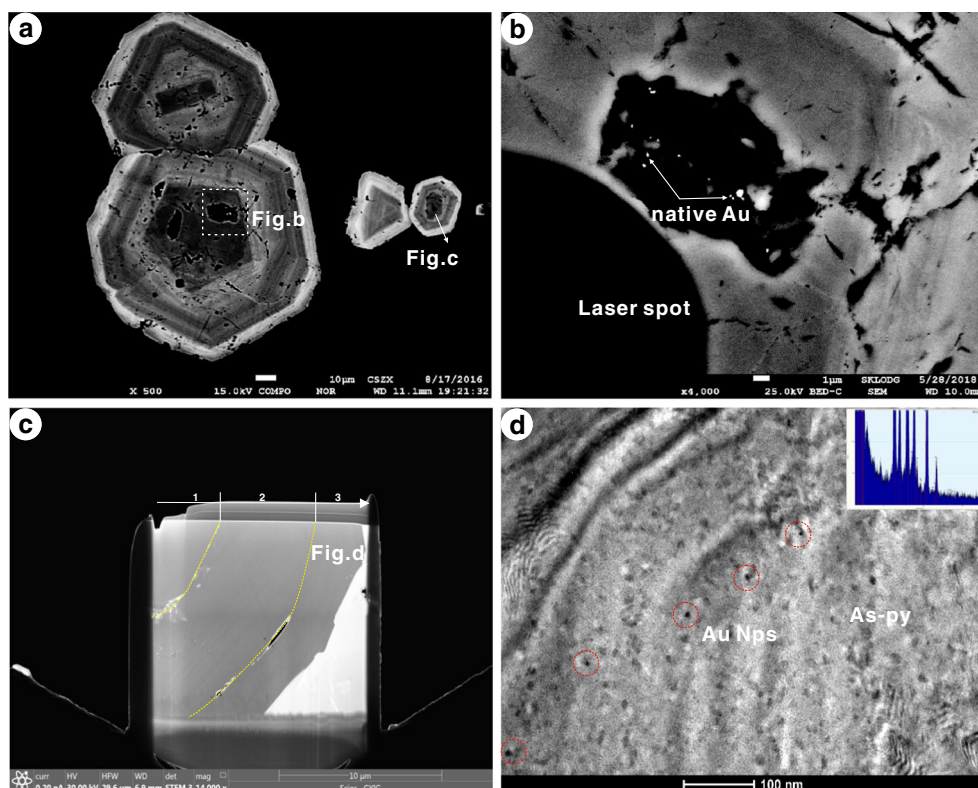
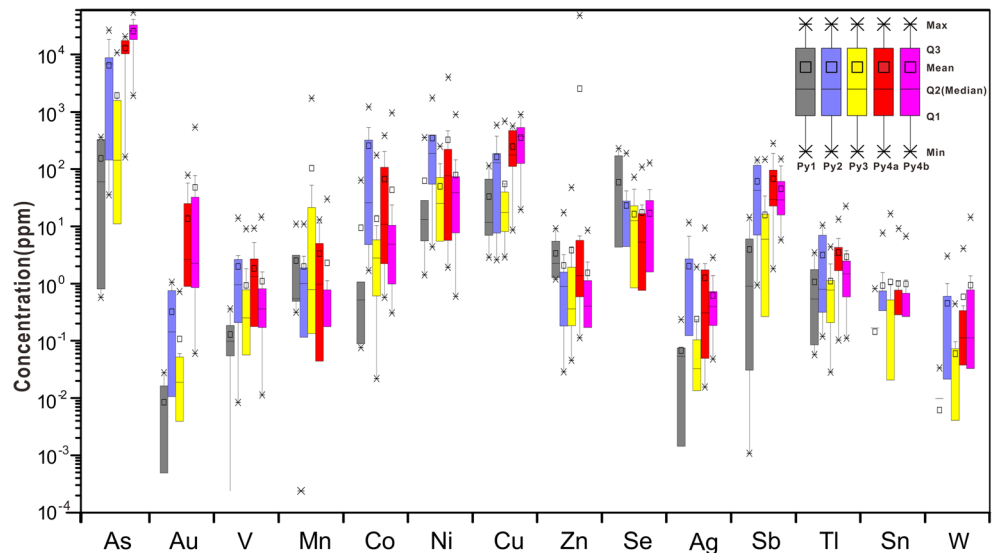


Fig. 9 Box plots showing trace element concentrations in the five pyrite types



538 ppm in Py4b. The average values of As concentrations increase from 59 ppm in Py1, 145 ppm in Py2, 144 ppm in Py3, 14,036 ppm in Py4a, to 25,978 ppm in Py4b. The maximum concentrations of As in Py4a and Py4b are as high as 17,959 ppm and 54,955 ppm, respectively (ESM Table 6, Figs. 9 and 10).

Nano-scale elemental and S-isotopic variation in pyrite

The spatial variations of relative abundances of ^{34}S and other selected elements such as Au, As, and Cu in individual grains of Py1b, Py3, and Py4b, determined by NanoSIMS mapping and line scan, are illustrated in Fig. 11 and ESM Fig. 3. On the basis of Au-As-Cu variations outward, both Py4a and Py4b can be further divided into three subzones (Py4a-1/Py4b-1, Py4a-2/Py4b-2, and Py4a-3/Py4b-3, Fig. 11 and ESM Fig. 3), respectively. Nearly simultaneous Py4a-1 and Py4b-1 are characterized by relatively high As and Cu but low Au contents; Py4a-2 and Py4b-2 are characterized by relatively high Au but low Cu contents; Py4a-3 and Py4b-3 are characterized by very low As, Au, and Cu contents than Py4a-2 and Py4b-2, possibly reflecting a waning stage of economic gold mineralization.

Subzones Py4a-1 and Py4b-1 are collectively characterized by approximately coherent variation of As and Cu. It is noteworthy to mention that As concentration in Py4a-2 and Py4b-2 are different. Py4a-2 is featured by decreased As than Py4a-1, holding a positive correlation between As and Cu, and a negative correlation between As and Au (ESM Fig. 3a). Differently, Py4b-2 is distinguished by increased As content compared with Py4b-1, with a generally positive but partly negative correlation between As and Au, a negative coherence between As (Au) and Cu (Fig. 11b, marked by dotted double sided arrow; ESM Fig. 3b, c, marked by orange dotted oval).

Discussion

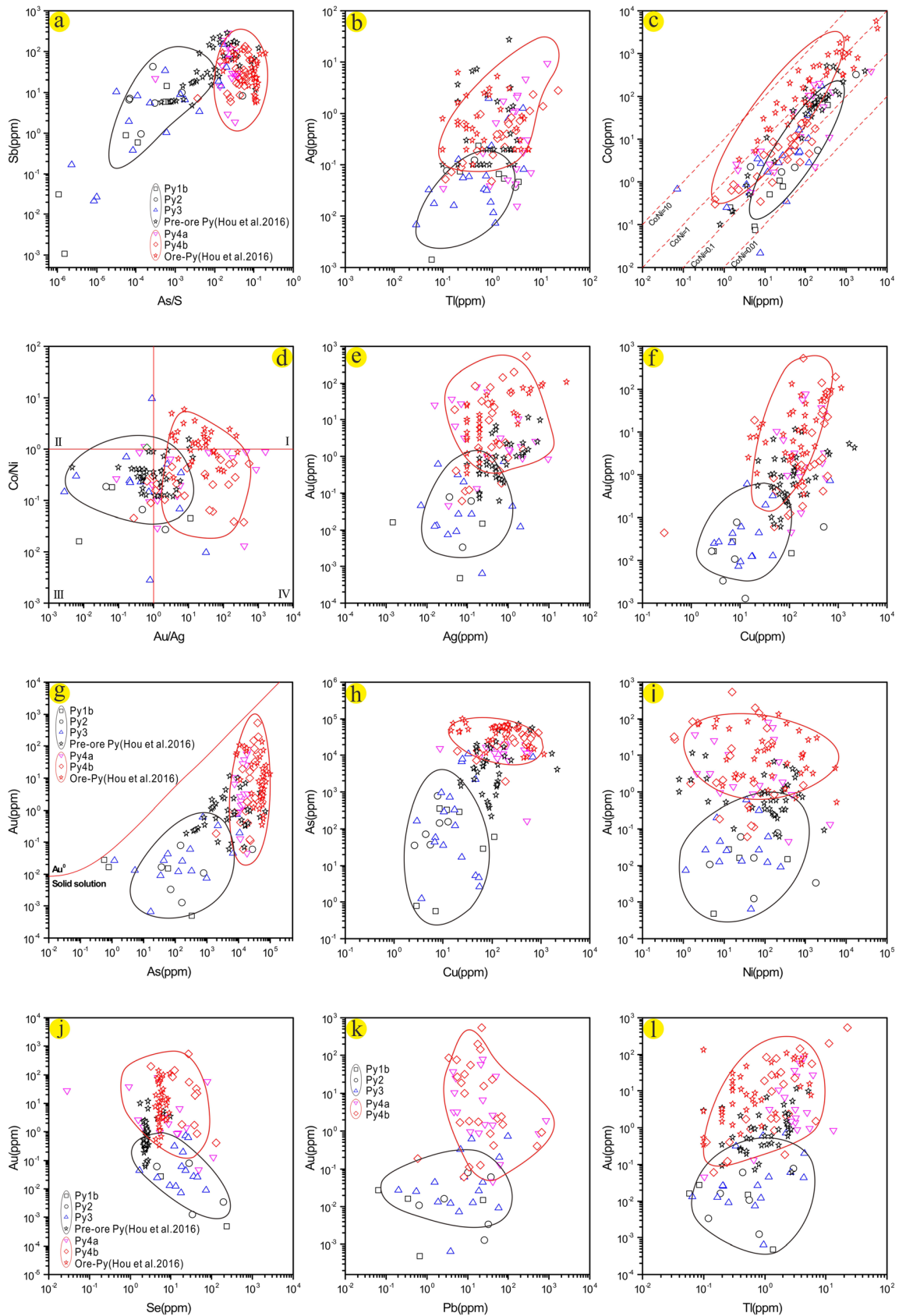
The mode of occurrence of gold

It has been suggested that Au in arsenian pyrite in CLGDs and some epithermal gold deposits worldwide is present in two forms, refractory as a substituting cation in the crystal texture and sub-micrometer to nanometer-size native gold particles or Au-Te aggregates (Simon et al. 1999; Palenik et al. 2004; Reich et al. 2005; Su et al. 2008, 2012).

LA-ICP-MS data elucidates that all spots are below the limit line of Au solubility (Fig. 10g; Reich et al. 2005), which implies Au mainly being a substituting cation in the crystal structure. If the experimental result is valid for all of the natural ore-forming systems, such phenomenon implies that the ore-forming fluids were not saturated with Au. However, clear Au spikes in Py4 are relatively rare in the NanoSIMS images but very common in the TEM image (Fig. 8). This, together with extremely large variation of Au concentration in Py4 determined by LA-ICP-MS and EPMA (Hou et al. 2016), indicate that at least some of Au in Py4 occur as Au nanoparticles (Au Nps). However, the ratio of these two different modes of occurrence of Au in the Shuiyindong gold deposit is yet to be determined and requires further research.

Gold precipitation mechanism

Boiling is an important mechanism for Au precipitation from ore fluid (Drummond and Ohmoto 1985), but in the Shuiyindong gold deposit, Au-bearing pyrite mostly associates with liquid-rich inclusions (Su et al. 2008), rather than aqueous liquid-rich inclusions coexisting with vapor-rich inclusions in the quartz. The scavenging of refractory Au from hydrothermal fluid is probably dominated by the kinetics of pyrite precipitation rather than equilibrium partitioning (Palenik et al. 2004). Surface



◀ **Fig. 10** Elemental binary plots for Py1–Py4, the black dotted polygons represent Py1–Py3, and the red dotted polygons represent Py4a and Py4b, respectively. **a** As/S vs. Sb, **b** Tl vs. Ag, **c** Ni vs. Co, **d** Au/Ag vs. Co/Ni, **e** Ag vs. Au, **f** Cu vs. Au, **g** As vs. Au, **h** Cu vs. As, **i** Ni vs. Au, **j** Se vs. Au, **k** Pb vs. Au, and **l** Tl vs. Au. Generally, As–Au–Cu–Sb–Tl–Ni–(Pb–Ag) element assemblages are enriched in Py4a and Py4b, and Se is abundant in Py1–Py3

and **2b**, Figs. **8b**, **11b**, and **12**; Reich et al. 2006; Large et al. 2011; Hou et al. 2016; Wu et al. 2019).

Pyrite compositional variation as indicators for fluid evolution

kinetics especially Fe-vacancies (i.e., the role of Fe-depleted, mineral surface) may contribute to the precipitation of Au (Deditius et al. 2014), which is consistent with the lower Fe content of Au-bearing pyrite than the theoretical value. During the deformation/metamorphism processes, the remobilization and redistribution of submicroscopic Au or Au Nps from crystal lattice of original pyrites by hydrothermal overprinting may also exist, as indicated by the occurrence of porous texture and microfractures in some of the Au-rich crystals (ESM Figs. **1h**, **i**

Chalcophile elements such as Co, Ni, As, and Se are commonly present in pyrite by substitution, with Ni–Co substituting Fe and As–Te substituting S (Zhang et al. 2014a). Thus, the variations of chalcophile elements in pyrite mainly reflect the variations of these elements in the parental fluids. Overall, the abundances of As–Au–Cu–Sb–Tl elements, As/S ratio, Co/Ni ratio, and Au/Ag ratio in the Au-rich pyrite (Py4) are significantly higher than those of the Au-poor pyrites (Py1, 2, 3) (Figs. **9** and **10**), indicating that the ore-forming fluids are distinctly enriched in As–Cu–Sb–Tl apart from Au. The variations of these trace elements are roughly

Fig. 11 NanoSIMS element mappings of representative pyrites. **a** Py4a from sample SYD-9a. **b–d** Py4b from sample SYD-5f. White squares represent the spot position for in situ sulfur isotope analysis and the white numbers show $\delta^{34}\text{S}$ values. Red words in white rectangles represent different pyrite stages and white arrows respond to line scans in ESM Fig. 3

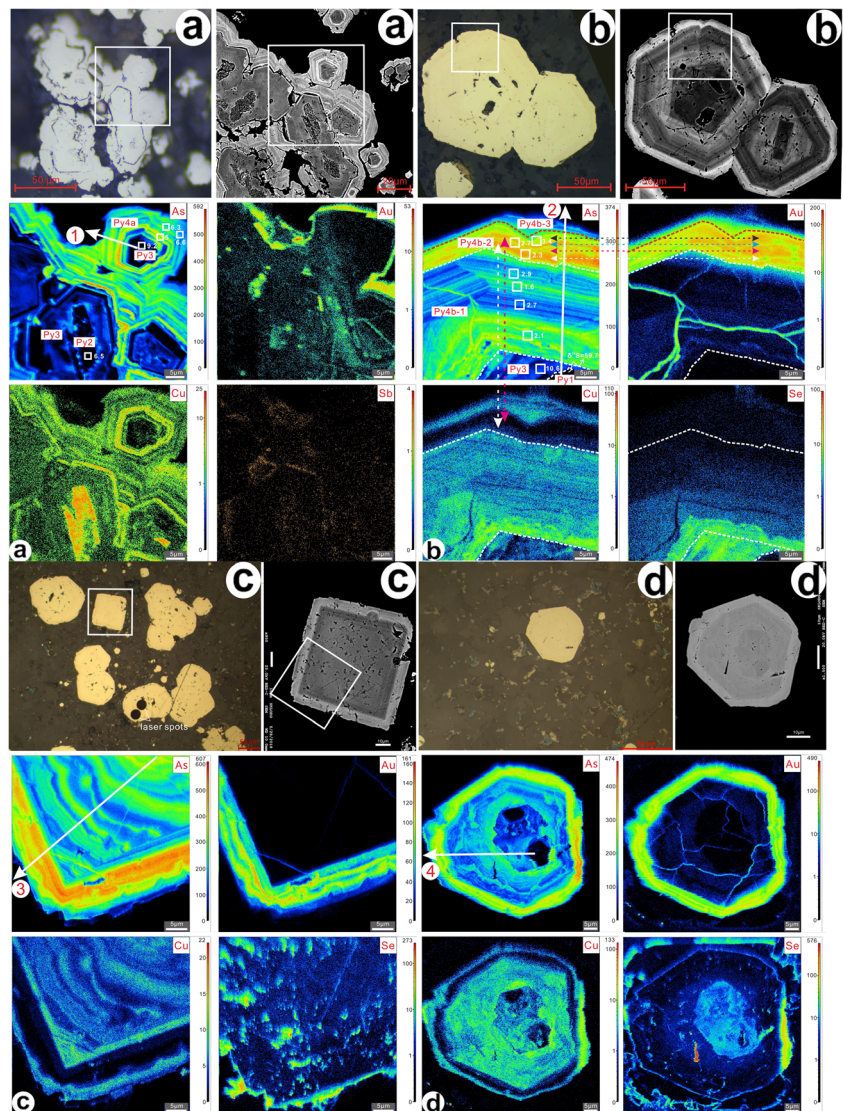
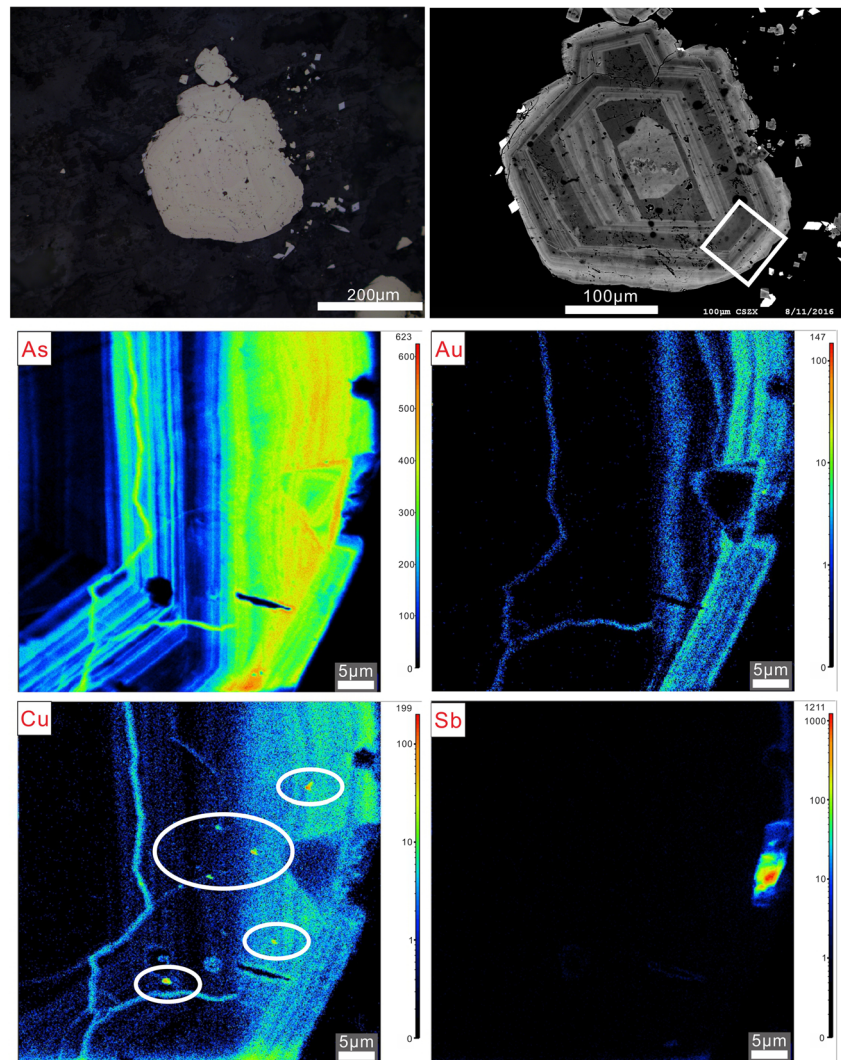


Fig. 12 Micro- to nano-sized particles of chalcopyrite dispersed as twinkling dots, from the sample SYD-2-8a



consistent with the range of data from Hou et al. (2016). However, unlike those described by Hou et al. (2016), our data show no huge overlap on Au concentrations between pre-ore and syn-ore pyrites. It is likely that this overlap was due to mixing of Py1 to Py3 and Py4.

The As-Au binary plot indicates that there are the lowest As concentrations (0.57–772 ppm) in Py1 and Py2, the middle values (1.2–10,894 ppm) in Py3, and the highest values (165–54,955 ppm) in Py4, respectively (ESM Table 6, Figs. 9 and 10). The Au-rich pyrites also have higher Au/Ag ratios (mostly 1~1000) than those of the Au-poor pyrites (mostly 0.01~1) (Fig. 10d).

The Co/Ni of pyrite is sensitive to environmental change and also a genetic indicator for some hydrothermal ore deposits (Eckert et al. 1979; Cook et al. 2009). In the Shuiyindong gold deposit, the Co/Ni ratios of Au-poor pyrites (Py1, 2, 3, mostly 0.01~0.1) and Au-rich pyrite (Py4, mostly 0.1~1) are significantly different (Fig. 10c). These two types of pyrite can be generally distinguished from each other in the plot of Co/Ni versus Au/Ag (Fig. 10d). The Au-rich pyrite with high Co/Ni ratios has been

attributed to an epizonogenic (epithermal) hydrothermal origin related to sedimentary facies by some researchers (Chen et al. 2009b; Li and Zeng 2005; Zhang et al. 2014a).

It's worth pointing out that the concentrations of Na, K, Al, Mg, and Si in pyrite, especially in the porous grains such as Py2, are highly variable, possibly due to the occurrence of carbonate, silicate, and clay inclusions in pyrite.

Sources of sulfur

Sulfur isotope composition of pyrite is a function of total sulfur composition, temperature, oxygen fugacity (fO_2), and acidity (pH) of the ore-forming fluid (Ohmoto 1972). With H_2S being the predominant sulfur species in hydrothermal fluids, sulfides crystallizing from hydrothermal solutions would have $\delta^{34}S$ values similar to the $\delta^{34}S_{\Sigma S}$ (Ohmoto and Goldhaber 1997; Chen et al. 2015b; Tan et al. 2015b), under the premise of no sulfates (e.g., gypsum and barite) coexisting with sulfide minerals in the deposit area.

The uncommon but rechecked high $\delta^{34}\text{S}$ values for Py1 have been rarely reported elsewhere, which were not detected by Hou et al. (2016), whose data were mostly within the range of -7.5 to $+7.9$ ‰ for pre-ore and ore pyrites. And the superheavy $\delta^{34}\text{S}$ values of Py1a (63.0–67.5‰) and Py1b (48.1–67.3‰) are within the wide range of sulfur isotopic fractionation (up to $\sim +75$ ‰) between the contemporary marine sulfate ($\sim +13$ ‰ for Permian) and sulfide, which is produced via the microbial sulfate reduction (MSR) process predicted by previous environmental studies and models (Canfield et al. 2010; Sim et al. 2011). For the $\delta^{34}\text{S}$ values of Py2 (2.4–7.6‰), Py3 (9.2–14.2‰) with the median at 4.8 and 11.2‰, they plot within the area of S isotope compositions from biogenic and abiogenic sulfate reduction (ESM Table 4; Fig. 7; Hou et al. 2016), and are close to the contemporary values of seawater sulfate (10–13‰; Fig. 7) under a relatively closed or not always open system (Ohmoto and Rye 1979).

Compared with Py1–Py3, Py4a (-1.2 to $+6.6$ ‰) and Py4b (-3.0 to $+5.8$ ‰) with the median at 3.7 and 2.7‰ have a narrow range (ESM Table 4; Fig. 6). They are roughly consistent with the $\delta^{34}\text{S}$ values of ore-related pyrite (-1.2 to $+1.5$ ‰, $n = 15$) and arsenopyrite (-0.8 to $+0.9$ ‰, $n = 8$) analyzed by SHRIMP, respectively (Hou et al. 2016). Using the isotope fractionation equation of Ohmoto (1972) and an average temperature of 220 °C estimated from fluid inclusions in quartz associated with Au mineralization from Su et al. (2012), the $\delta^{34}\text{S}$ values of H_2S in the ore-forming fluids crystallizing the Au-rich pyrite (3.1‰ average) are estimated to fluctuate around 1.5‰. It is worth to note that late ore-related sulfide minerals including stibnite, realgar, and orpiment have very similar $\delta^{34}\text{S}$ values, which are tabulated between -5 and $+5$ ‰ (ESM Table 4; Zhang et al. 2010; Wang et al. 2013; Tan et al. 2015b; Hou et al. 2016) and suggest a homogenous source of sulfur.

The homogenous and narrow sulfur isotopic compositions preclude the possibility that the sulfur is from sedimentary rocks, whereas indicating either a magmatic or deep metamorphic origin (Ohmoto 1986; Groves et al. 2003; Chang et al. 2008; Xie et al. 2018). Due to the paucity of contemporary igneous rocks within the Youjiang basin, no sufficient evidence supports a magmatic source. The rarely exposed igneous rocks are constituted of late Permian diabase (~ 259 Ma; Zhang and Xiao 2014), felsic and ultramafic dikes at the basin margins (77.4–99.4 Ma; Liu et al. 2010; Chen et al. 2012, 2014; Zhu et al. 2017), which are not consistent with the mineralization age in SW Guizhou Province (~ 140 Ma; Su et al. 2009a; Wang 2013; Chen et al. 2019). Hydrothermal pyrite, arsenopyrite, and stibnite collected from the Zhesang, Badu, Yata, and also Shuiyindong gold deposits got very low $^3\text{He}/^4\text{He}$ value (0.01–0.05 Ra, unpublished data) by other research of our group recently, which indicate that the contribution of magma is negligible. Therefore, the sulfur of ore-forming fluid was not probably dominated by magmatic origin and thus different from that of CLGDs in Nevada, which are approximately contemporaneous with calc-alkalic magmatism (Hu et al. 2002; Kesler et al. 2005; Muntean et al. 2011).

Therefore, a deep metamorphic origin might be the only candidate for the sulfur source. There are a few observations to support such hypothesis as below. (1) During the Late Indosinian and Yanshanian orogenies, regional metamorphism has occurred in the Youjiang basin (Su et al. 2009b, 2018). Most of the exposed Triassic strata have regionally experienced low-grade burial metamorphism (anchizone to epizone), overlying Proterozoic low-grade metamorphic basement rocks (Wang et al. 1995; Suo et al. 1998; Su et al. 2009b). The evidences from H-O isotope compositions and CO_2 -enriched feature of ore fluids imply a metamorphic origin, probably associated with crustal thickening and prograde metamorphism (Hofstra et al. 2005; Su et al. 2009b). (2) As observed by Hou et al. (2016), pressure shadows were developed in ore-stage pyrite-quartz veinlets, ascribed to deformation and metamorphism (Large et al. 2007). (3) The variations of sulfur isotopes of pyrites from pre-ore to ore stages can be used to reflect metamorphic process. Previous study indicated that the ranges of $\delta^{34}\text{S}$ values of pyrites from early to late stage were successively narrower, which resulted from gradual homogenization of S during metamorphism (Large et al. 2007; Chang et al. 2008). Similar narrowing trend can also be found in this study, with ranges of $\delta^{34}\text{S}$ values (ESM Table 4) decreasing from Py1 (-37.5 to $+67.5$ ‰; Zhao et al. 2018), to Py2–Py3 ($+2.4$ to $+14.2$ ‰), to Py4 (-3.0 to $+6.6$ ‰), and to late sulfides (stibnite and realgar; $+1.6$ to $+3.0$ ‰; this study). (4) During deformation or metamorphism, lattice-bound gold could be released to form Au nanoparticles and even native gold in the later pyrite generations (Large et al. 2007), in good agreement with the microscopic and TEM observations in this study and Su et al. (2008, 2012). In summary, the combination of sulfur isotopic studies and geological observations suggests that S of Py4 implies a metamorphic source.

Potentially, the fluid oxidized by meteoric water or physicochemical changes (e.g., brecciation and subsequent pressure fluctuations, Fig. 4e) may exert significant effects on decreasing (>25 ‰–40‰) or even negative $\delta^{34}\text{S}$ values of sulfides during the mineralization processes (Goldhaber et al. 1978; Hodkiewicz et al. 2009; LaFlamme et al. 2016; Wu et al. 2019). Accordingly, the fractionation of heavy ^{34}S into the oxidized sulfur species (e.g., barite) would lead to ^{32}S -enriched H_2S in the residual ore fluid, and subsequent precipitation of decreased- $\delta^{34}\text{S}$ sulfides (e.g., pyrite or marcasite) (Ohmoto 1972; Wu et al. 2019). The decreasing $\delta^{34}\text{S}$ values of Au-rich pyrite (Py4) from strata-bound orebodies No. I to No. V can be attributed to the fluid oxidation resulted from meteoric fluid mixing, demonstrated by the H-O isotope analysis of fluid inclusions in quartz (Hu et al. 2002; Wang 2013; Peng et al. 2014; Tan et al. 2015b). And the mixing ratio between upward hydrothermal fluid and downward meteoric water is negatively correlated with depth.

To sum up, S of Py4 may have originated from a dominant metamorphic reservoir, but $\delta^{34}\text{S}$ values of sulfides can be altered by the increasing mixing degree of meteoric water

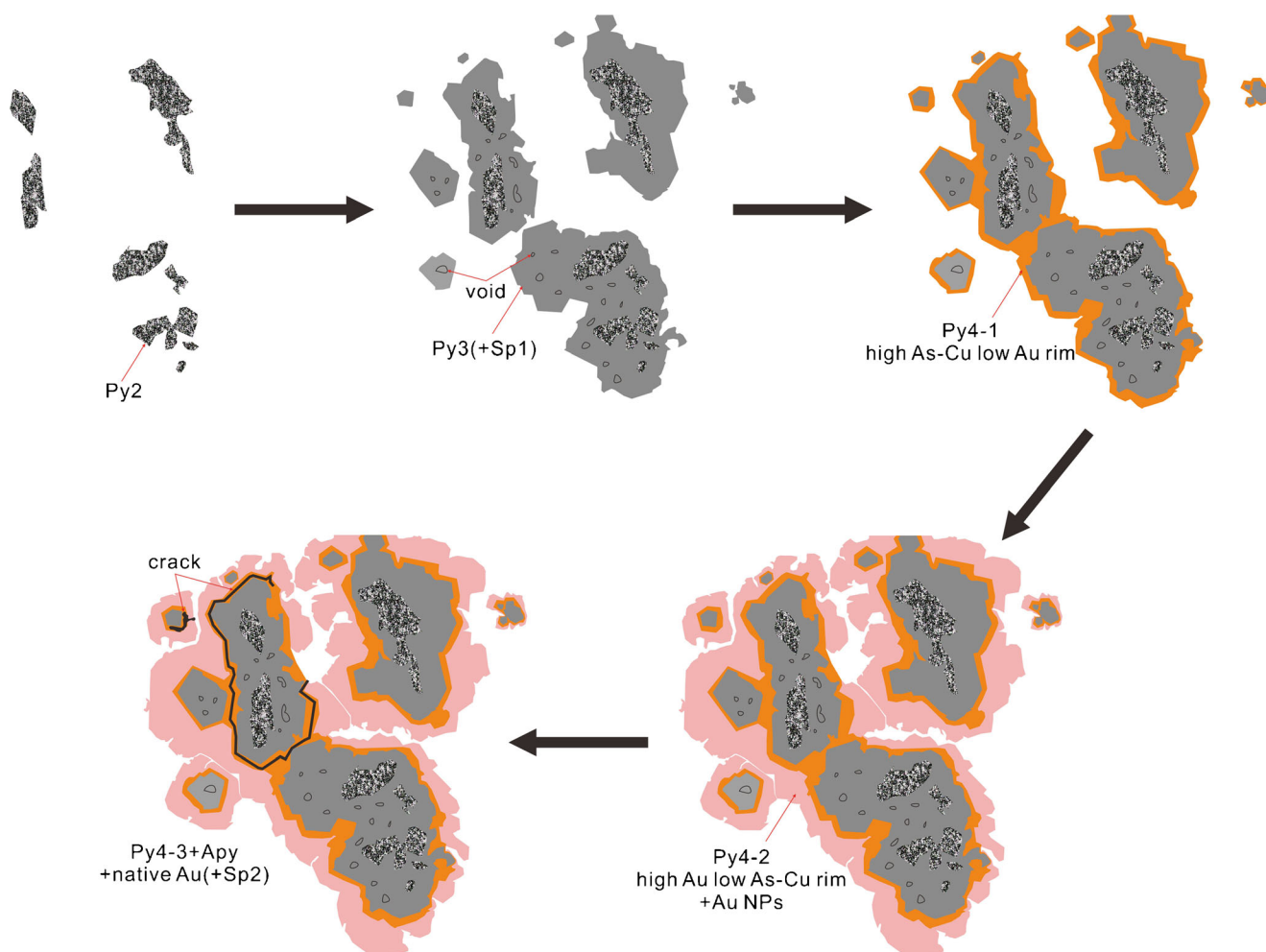


Fig. 13 A cartoon illustrating the different stages of Py2 to Py4 (substages included)

upward. The isotopic fractionation ascribed to the change of geochemical conditions such as fluid oxidation cannot be precluded. Given that both sulfur and ore-forming fluids have a metamorphic origin, gold might be released by metamorphic fluids and transported as S-bearing complexes (Groves et al. 2003; Chang et al. 2008). Then as proposed by Su et al. (2018), the ore-forming fluids uplift following reactivated basement-penetrating rift faults and gold precipitations occurred in favorable locality. If the scenario is correct, we can boldly extrapolate the explanation to the southeastern Guizhou especially Huijiangbao anticline district.

Nano-scale elemental and S-isotopic variation in pyrite

Differences in the elemental zoning of gold and other trace elements across individual pyrite grains are interpreted to represent the influx and evolution of ore fluids (Barker et al. 2009). Delineation of vertical and lateral $\delta^{34}\text{S}$ distribution patterns of ore-related Py4a/Py4b in the Shuiyindong gold

deposit is essential for understanding the potential upward and lateral migration processes of ore-forming fluids, and for predicting undiscovered orebodies and establishing of exploration model. The coupled geochemistry of Au and As in pyrite is an ubiquitous phenomenon in wide range of hydrothermal and diagenetic environments (Deditius et al. 2014). We tried to compare the differences of Py4a and Py4b by NanoSIMS line and plane scans reflecting the variation in trace element distribution (Figs. 11 and 12; ESM Fig. 3), especially for As-Au-Cu.

Py4a-2 and partial Py4b-2 show a decoupled behavior of As and Au (ESM Fig. 3a–c), which can be interpreted by the possibilities summarized by Li et al. (2019): (1) Au is also incorporated via absorption-chemisorption of invisible nanoparticles of Au (Au^0) on the pyrite surface during growth (Palenik et al. 2004; Li et al. 2019). This is in accordance with the occurrence of Au Nps detected by TEM. (2) The disequilibrium incorporation of Au and As can be resulted from the rapid growth of pyrite (Fougereuse et al. 2016), which results in the different availabilities of Au and As from solution

(Li et al. 2019). (3) As may not be essential for the incorporation of invisible Au, and even As-free pyrites can also contain Au, which was reported by Cook et al. (2009) and Ciobanu et al. (2012).

Au and Cu of Py4a-2 and Py4b-2 always indicate a negative correlation, which may be explained by the reasons as follows: (1) Au^{3+} may occur dominantly when the pH increase and the condition is more oxidized during the evolution of ore fluids, which could allow the substitute of Au^{3+} with Cu^{2+} (Yan et al. 2018); (2) increasing fluid temperature from inner zone to outer zone leads to decreasing solubility of Au, Cu, and As in pyrite, which leads to the expulsion of As (Au), Cu from pyrite and subsequent incorporation in sulfide phases such as late-stage chalcopyrite, Pb-Sb-sulfosalt, and sphalerite (Fig. 12; Zygouri et al. 2017). It probably implies that Au and Cu are structurally bound in zone Py4-1, structurally bound or submicron-sized Au-rich/Cu-sulfide particles in zone Py4-2, whereas the As is in solid solution in both zones as discussed above. Increasing fluid temperature from Py4-1 to Py4-2 zone leads to decreasing solubility of Au, Cu, and As in pyrite, resulting in partial expulsion of As from pyrite, which is indicated by a decoupled partly correlation of As and Au of zone Py4b-2.

In consideration of the decoupling of Cu and As in Py4b-2 (ESM Fig. 3b), it may be explained that Cu can occur as both solid solution and micro- to nano-sized particles of chalcopyrite (Fig. 12; Reich et al. 2013) while As mainly occurs structurally bound in pyrite. Tardani et al. (2017) reported that pyrites from the shallow argillic zone have As (Cu) zonation and a decoupled phenomenon of As and Cu, due to the separation of single-phase fluid into a low-density vapor depleted in As/Cu ratio, and a denser brine enriched in As/Cu ratio, which is able to fractionate As and Cu. However, the aforementioned element zoning is not symmetric but secular, embodied in one element locally enriched but depleted in other positions even along the same overgrowth rim (Fig. 11b–d). That might be resulted from the selective partitioning of metals into the pyrite owing to physicochemical changes in ore-forming fluid (Deditius et al. 2009). The heterogeneous $\delta^{34}\text{S}$ values of various stages registered from core to rim of each individual pyrite grain are shown in Fig. 11a, b. Taking an example of Py4 in ESM Fig. 1c (Py1 is not included), we use a cartoon illustrating the overgrowing and overprinting features for various stages and subzones of pyrite formation (Fig. 13), expounding the As-Au-Cu elemental variation systematically.

Notably, compared with zone Py4a-2 holding a single intensity peak for Py4a (ESM Fig. 3a), Py4b-2 always carry four peaks at most (ESM Fig. 3b), which probably coincides with different periodic replenishment of ore-forming fluids. The Py4a-2 is mainly resulted from a sharp drop in either pressure or temperature near the fault passage, and the Py4b-2 is mainly because of a stable and sustainable fluid environment. Even

from the same thin section, two peaks or three peaks of different pyrites indeed occur unevenly and discontinuously (ESM Fig. 3c, d), probably on account of the difference of fluid unloading and metal precipitation in different individual particles.

Integrated variations in $\delta^{34}\text{S}$ and As-Au-Cu correlations reflect that pyrite growth is accompanied by gradual changes and consequent variations in fluid geochemistry along the migration pathway on the macro level. Although in this scenario, the exact precipitation mechanism still remains open. However, what is clear is that the Shuiyindong gold deposit underwent physicochemical changes of aqueous and/or aqueous-carbonic fluids along migration paths, probably causing the destabilization of Au-bisulfide complexes during local fluid-rock interactions (e.g., sulfidation) of carbonate wall rocks (Deditius et al. 2014).

Conclusion

1. Four types of pyrite are present in the Shuiyindong gold deposit. The As-rich pyrite (Py4) contains higher Au, Cu, Sb, and Tl than the As-poor pyrites (Py1, Py2, and Py3). This, together with TEM observation, indicates that some of the Au in Py4 is present as nanoparticles.
2. The $\delta^{34}\text{S}$ values of Py4 from five different orebodies vary from 4.1 to 1.3‰ averagely. Although these values overlap the range of typical magmatic values, the evidence of few coeval magmatic rocks in the district and decreasing variations of $\delta^{34}\text{S}$ values from Py1 to Py4 may discount the magmatic origin but suggests that sulfur of Py4 implies a metamorphic source.
3. Our data support the notion that the metamorphic fluid mixed by meteoric water might play a critical role in ore formation. Alternatively, the fluid oxidation can also result in the large fractionation of sulfur isotopes.
4. Integrated variations in $\delta^{34}\text{S}$ and As-Au-Cu correlations infer the physicochemical changes of aqueous and/or aqueous-carbonic fluids along migration paths.

Acknowledgments This study was funded by the National 973 Program of China (2014CB440906) and the National Natural Foundation of China (41830432, U1812402). We thank Guizhou Zijin Gold Mines for field work support. We are grateful to Mr. Jianchao Zhang and Mr. Jialong Hao for helping with NanoSIMS S isotope analyses, to Mr. Wei Gao for helping with LA-ICP-MS analyses, to Ms. Rui Li for FIB work, and to Dr. Shirong Liu for TEM tests, respectively. Big thanks are given to Dr. Chusi Li of Indiana University for English language polishing for the early version of this manuscript. We acknowledge all the reviewers including Dr. Ross R. Large (University of Tasmania) and an anonymous reviewer for their constructive reviews and considerate suggestions that led to great improvement of this paper. We also would like to thank Editor-in-Chief Bernd Lehmann and associate editor Shao-yong Jiang for handling our manuscript.

References

- Arehart GB (1996) Characteristics and origin of sediment-hosted disseminated gold deposits: a review. *Ore Geol Rev* 11:383–403
- Ashley RP, Cunningham CG, Bostick NH, Dean WE, Chou IM (1991) Geology and geochemistry of three sedimentary-rock-hosted disseminated gold deposits in Guizhou Province, People's Republic of China. *Ore Geol Rev* 6:133–151
- Barker SLL, Hickey KA, Cline JS, Dipple GM, Kilburn MR, Vaughan JR, Longo AA (2009) Uncovering invisible gold: use of nanosims to evaluate gold, trace elements, and sulfur isotopes in Pyrite from Carlin-Type Gold Deposits. *Econ Geol* 104:897–904
- Canfield DE, Farquhar J, Zerkle AL (2010) High isotope fractionations during sulfate reduction in a low-sulfate euxinic ocean analog. *Geology* 38:415–418
- Chang ZS, Large RR, Maslennikov V (2008) Sulfur isotopes in sediment-hosted orogenic gold deposits: Evidence for an early timing and a seawater sulfur source. *Geology* 36:971–974
- Chen MH, Huang QW, Hu Y, Chen ZY, Zhang W (2009a) Genetic types of phyllosilicate (micas) and its Ar-Ar dating in Lannigou gold deposit, Guizhou Province, China. *Acta Mineral Sin* 29:353–362 (in Chinese with English abstract)
- Chen YJ, Zhai MG, Jiang SY (2009b) Significant achievements and open issues in study of orogenesis and metallogenesis surrounding the North China continent. *Acta Petrol Sin* 25:2695–2726
- Chen MH, Lu G, Li XH (2012) Muscovite $^{40}\text{Ar}/^{39}\text{Ar}$ dating of the quartz porphyry veins from Northwest Guangxi, China, and its geological significance. *Geol J China Univ* 18(1):106–116 (in Chinese with English abstract)
- Chen MH, Zhang Y, Meng YY, Lu G, Liu SQ (2014) Determination of upper limit of metallogenic epoch of Liaotun gold deposit in western Guangxi and its implications for chronology of Carlin-type gold deposits in Yunnan-Guizhou-Guangxi “golden triangle” area. *Mineral Deposits* 1:1–13 (in Chinese with English abstract)
- Chen MH, Mao JW, Li C, Zhang ZQ, Dang Y (2015a) Re-Os isochron ages for arsenopyrite from Carlin-like gold deposits in the Yunnan-Guizhou-Guangxi “golden triangle”, southwestern China. *Ore Geol Rev* 64:316–327
- Chen MH, Zhang ZQ, Santosh M, Dang Y, Zhang W (2015b) The Carlin-type gold deposits of the “golden triangle” of SW China: Pb and S isotopic constraints for the ore genesis. *J Asian Earth Sci* 103:115–128
- Chen MH, Bagas L, Liao X, Zhang ZQ, Li QL (2019) Hydrothermal apatite SIMS Th-Pb dating: constraints on the timing of low-temperature hydrothermal Au deposits in Nibao, SW China. *Lithos* 324-325:418–428
- Ciobanu CL, Cook NJ, Utsunomiya S, Kogagwa M, Green L, Gilbert S, Wade B (2012) Gold-telluride nanoparticles revealed in arsenic-free pyrite. *Am Mineral* 97:1515–1518
- Cline JS, Hofstra AH, Muntean JL, Tosdal RM, Hickey KA (2005) Carlin-type gold deposits in Nevada: Critical geologic characteristics and viable models. *Econ Geol* 100th anniversary volume 100: 451–484
- Cline JS, Muntean JL, Gu XX, Xia Y (2013) A comparison of Carlin-type gold deposits: Guizhou Province, golden triangle, southwest China, and northern Nevada, USA. *Front Earth Sci* 20:1–18
- Cook NJ, Ciobanu CL, Mao JW (2009) Textural control on gold distribution in As-free pyrite from the Dongping, Huangtuliang and Hougou gold deposits, North China Craton (Hebei Province, China). *Chem Geol* 264:101–121
- Deditius AP, Utsunomiya S, Ewing RC, Chryssoulis SL, Venter D, Kesler SE (2009) Decoupled geochemical behavior of As and Cu in hydrothermal systems. *Geology* 37(8):707–710
- Deditius AP, Reich M, Kesler SE, Utsunomiya S, Chryssoulis SL, Walshe J, Ewing RC (2014) The coupled geochemistry of Au and As in pyrite from hydrothermal ore deposits. *Geochim Cosmochim Acta* 140:644–670
- Drummond SE, Ohmoto H (1985) Chemical evolution and mineral deposition in boiling hydrothermal systems. *Econ Geol* 80:126–147
- Du YS, Huang H, Yang JH, Huang HW, Tao P, Huang ZQ, Hu LS, Xie CX (2013) The basin translation from Late Paleozoic to Triassic of the Youjiang basin and its tectonic signification. *Geological Review* 59:1–11 (in Chinese with English abstract)
- Eckert T, Barnes A, Dhawan V, Frucht S (1979) A reevaluation of the Co/Ni ratio in pyrite as geochemical tool in ore genesis problems. *Mineral Deposita* 14:353–374
- Feng JR, Mao JW, Pei RF, Li C (2011) A tentative discussion on Indosinian ore-forming events in Laojunshan area of southeastern Yunnan: A case study of Xinzhai tin deposit and Nanyangtian tungsten deposit. *Mineral Deposits* 30(01):57–73 (in Chinese with English abstract)
- Fougerouse D, Reddy SM, Saxey DW, Rickard WD, Van Riessen A, Micklethwaite S (2016) Nanoscale gold clusters in arsenopyrite controlled by growth rate not concentration: evidence from atom probe microscopy. *Am Mineral* 101:1916–1919
- Goldhaber MB, Reynolds RL, Rye RO (1978) Origin of a South Texas roll-type deposit; II, Sulfide petrology and sulfur isotope studies. *Econ Geol* 73:1690–1705
- Groves DI, Goldfarb RJ, Robert F, Hart CJR (2003) Gold deposits in metamorphic belts: overview of current understanding, outstanding problems, future research, and exploration significance. *Econ Geol Bull Soc Econ Geol* 98:1–29
- Guo ZC, Zhou ZF (2006) Exploration practice of Huijiabao-anticline gold deposit, southwest Guizhou and establishment on two-story-building model. *Guizhou Geology* 3:176–181 (in Chinese with English abstract)
- Hodkiewicz PF, Groves DI, Davidson GJ, Weinberg RF, Hagemann SG (2009) Influence of structural setting on sulphur isotopes in Archean orogenic gold deposits, Eastern Goldfields Province, Yilgarn, Western Australia. *Mineral Deposita* 44:129–150
- Hofstra AH, Cline JS (2000) Characteristics and models for Carlin-type gold deposits. *Rev Econ Geol* 13:163–220
- Hofstra AH, Zhang XC, Emsbo P, Hu RZ, Su WC, Christiansen WD, Fu SH (2005) Source of ore fluids in Carlin-type gold deposits in the Dian-Qian-Gui area and West Qinling belt, PR China: Implications for genetic models. *Mineral Deposit Research: Meeting the Global Challenge*. Springer Berlin Heidelberg 533–536
- Hou L, Peng HJ, Ding J, Zhang JR, Zhu SB, Wu SY et al (2016) Textures and in situ chemical and isotopic analyses of pyrite, Huijiabao trend, Youjiang basin, China: Implications for paragenesis and source of sulfur. *Econ Geol* 111:331–353
- Hu RZ, Zhou MF (2012) Multiple Mesozoic mineralization events in South China—an introduction to the thematic issue. *Mineral Deposita* 47:579–588
- Hu RZ, Su WC, Bi XW, Tu GZ, Hofstra AH (2002) Geology and geochemistry of Carlin-type gold deposits in China. *Mineral Deposita* 37:378–392
- Hu ZC, Zhang W, Liu YS, Gao S, Li M, Zong KQ, Chen HH, Hu SH (2015) “Wave” signal-smoothing and mercury-removing device for laser ablation quadrupole and multiple collector ICPMS analysis: application to lead isotope analysis. *Anal Chem* 87:1152–1157
- Hu RZ, Fu SL, Huang Y, Zhou MF, Fu SH, Zhao CH et al (2017a) The giant South China Mesozoic low-temperature metallogenic domain: Reviews and a new geodynamic model. *J Asian Earth Sci* 137:9–34
- Hu RZ, Chen WT, Xu DR, Zhou MF (2017b) Reviews and new metallogenic models of mineral deposits in South China: An introduction. *J Asian Earth Sci* 137:1–8
- Kesler SE, Riciputi LC, Ye ZJ (2005) Evidence for a magmatic origin for Carlin-type gold deposits: isotopic composition of sulfur in the Betze-Post-Screamer Deposit, Nevada, USA. *Mineral Deposita* 40: 127–136

- LaFlamme C, Martin L, Jeon H, Reddy S, Selvaraja V, Caruso S, Hao TB, Roberts MP, Voute F, Hagemann S, Wacey D, Littman S, Wing B, Fiorentini M, Kilburn MR (2016) In situ multiple sulfur isotope analysis by SIMS of pyrrhotite, pentlandite and chalcopyrite to refine magmatic ore genetic models. *Chem Geol* 444:1–15
- Large RR, Maslennikov VV, Robert F, Danyushevsky LV, Chang ZS (2007) Multistage sedimentary and metamorphic origin of pyrite and gold in the giant Sukhoi log deposit, Lena gold province, Russia. *Econ Geol* 7:1233–1267
- Large RR, Bull SW, Maslennikov VV (2011) A carbonaceous sedimentary source-rock model for Carlin-type and orogenic gold deposits. *Econ Geol* 3:331–358
- Li HB, Zeng FZ (2005) The pyrite's typomorphic characteristics in gold deposit. *Contributions to Geology and Mineral Resources Research* 20:199–203 (in Chinese with English abstract)
- Li W, Cook NJ, Xie GQ, Mao JW, Ciobanu CL, Li JW, Zhang ZY (2019) Textures and trace element signatures of pyrite and arsenopyrite from the Gutaishan Au–Sb deposit, South China. *Mineral Deposita* 54(4):591–610
- Liu JZ (2001) The Geology of the Yanshang Gold Deposit, Zhenfeng County, Guizhou. *Guizhou Geology* 3:174–178 (in Chinese with English abstract)
- Liu JZ, Liu CQ (2005) Origin and metallogenic model for Shuiyindong gold deposit of Guizhou. *Guizhou Geology* 22:9–13 (in Chinese with English abstract)
- Liu JM, Ye J, Ying HL, Liu J, Zheng MH, Gu XX (2002) Sediment-hosted micro-disseminated gold mineralization constrained by basin paleo-topographic highs in the Youjiang basin, South China. *J Asian Earth Sci* 20:517–533
- Liu JZ, Deng YM, Liu CQ, Xia Y, Zhang XC, Tao Y (2006a) Geochemical studies on the inclusion and isotopes of the Shuiyindong gold deposit. *Guizhou Geology* 23:51–56 (in Chinese with English abstract)
- Liu JZ, Deng YM, Liu CQ, Zhang XC, Xia Y (2006b) Metallogenic conditions and model of the superlarge Shuiyindong stratabound gold deposit in Zhenfeng County, Guizhou Province. *Geol China* 33:169–177 (in Chinese with English abstract)
- Liu YS, Hu ZC, Gao S, Günther D, Xu J, Gao CG, Chen HH (2008) In situ analysis of major and trace elements of anhydrous minerals by LA-ICP-MS without applying an internal standard. *Chem Geol* 257:34–43
- Liu S, Su WC, Hu RZ, Feng CX, Gao S, Coulson IM, Wang T, Feng GY, Tao Y, Xia Y (2010) Geochronological and geochemical constraints on the petrogenesis of alkaline ultramafic dikes from southwest Guizhou Province, SW China. *Lithos* 114:253–264
- Mao JW, Cheng YB, Chen MH, Pirajno F (2013) Major types and time-space distribution of Mesozoic ore deposits in South China and their geodynamic settings. *Mineral Deposita* 48:267–294
- Muntean JL, Cline JS, Simon AC, Longo AA (2011) Magmatic-hydrothermal origin of Nevada's Carlin-type gold deposits. *Nat Geosci* 4:122–127
- Murochick JB (1992) Marcasite inversion and the petrographic determination of pyrite ancestry. *Econ Geol* 87:1141–1152
- Nevolko PA, Hoa TT, Redin YO, Anh TT, Phuong NT et al (2017) Geology, mineralogy, geochemistry and $\delta^{34}\text{S}$ of sedimentary rock-hosted Au deposits in Song Hien structure, NE Vietnam. *Ore Geol Rev* 84:273–288
- Ohmoto H (1972) Systematics of sulfur and carbon isotopes in hydrothermal ore deposits. *Econ Geol* 67:551–578
- Ohmoto H (1986) Stable isotope geochemistry of ore deposits: Reviews in Mineralogy 16:491–559
- Ohmoto H, Goldhaber MB (1997) Sulfur and carbon isotopes. *Geochemistry of hydrothermal ore deposits*, 3rd edn. Wiley, New York, pp 517–611
- Ohmoto H, Rye RO (1979) Isotopes of sulfur and carbon. In: Barnes HL (ed) *Geochemistry of hydrothermal ore deposits*. Wiley, New York, pp 509–567
- Palenik CS, Utsunomiya S, Reich M, Kesler SE, Wang LM, Ewing RC (2004) Invisible gold revealed: Direct imaging of gold nanoparticles in a Carlin-type deposit. *Am Mineral* 89:1359–1366
- Peng YW, Gu XX, Zhang YM, Liu L, Wu CY, Chen SY (2014) Source and evolution of ore-forming fluid of the Huijiabao gold field, Southwestern Guizhou: evidences from fluid inclusions and stable isotopes. *Bull Mineral Petrol Geochem* 33:666–680
- Peters SG, Huang JZ, Li ZP, Jing CG (2007) Sedimentary rock-hosted Au deposits of the Dian-Qian-Gui area, Guizhou, and Yunnan Provinces, and Guangxi District, China. *Ore Geol Rev* 31:170–204
- Pi QH, Hu RZ, Peng KQ, Wu JB, Wei CW, Huang Y (2016) Geochronology of the Zhesang gold deposit and mafic rock in Funing County of Yunnan Province, with special reference to the dynamic background of Carlin-type gold deposits in the Dian-Qian-Gui region. *Acta Petrol Sin* 32(11):3321–3342
- Pi QH, Hu RZ, Xiong B, Li QL, Zhong RC (2017) In situ SIMS U-Pb dating of hydrothermal rutile: reliable age for the Zhesang Carlin-type gold deposit in the golden triangle region, SW China. *Mineral Deposita* 52:1179–1190
- Reich M, Kesler SE, Utsunomiya S, Palenik CS, Chryssoulis SL, Ewing RC (2005) Solubility of gold in arsenian pyrite. *Geochim Cosmochim Acta* 69:2781–2796
- Reich M, Utsunomiya S, Kesler SE, Wang LM, Ewing RC, Becker U (2006) Thermal behavior of metal nanoparticles in geologic materials. *Geology* 34:1033–1036
- Reich M, Deditius AP, Chryssoulis S, Li JW, Ma CQ, Parada MA et al (2013) Pyrite as a record of hydrothermal fluid evolution in a porphyry copper system: a SIMS/EMPA trace element study. *Geochim Cosmochim Acta* 104:42–62
- Sim MS, Bosak T, Ono S (2011) Large sulfur isotope fractionation does not require disproportionation. *Science* 333(6038):74–77
- Simon G, Huang H, Pennerhahn JE, Kesler SE, Kao LS (1999) Oxidation state of gold and arsenic in gold-bearing arsenian pyrite. *Am Mineral* 84:1071–1079
- Su WC, Xia B, Zhang HT, Zhang XC, Hu RZ (2008) Visible gold in arsenian pyrite at the Shuiyindong Carlin-type gold deposit, Guizhou, China: implications for the environment and processes of ore formation. *Ore Geol Rev* 33:667–679
- Su WC, Hu RZ, Xia B, Xia Y, Liu YP (2009a) Calcite Sm-Nd isochron age of the Shuiyindong Carlin-type gold deposit, Guizhou, China. *Chem Geol* 258:269–274
- Su WC, Heinrich CA, Pettke T, Zhang XC, Hu RZ, Xia B (2009b) Sediment-hosted gold deposits in Guizhou, China: products of wall-rock sulfidation by deep crustal fluids. *Econ Geol* 104:73–93
- Su WC, Hu RZ, Ge X, Xia B, Chen YY, Zhu C (2012) Mineralogy and geochemistry of gold-bearing arsenian pyrite from the Shuiyindong Carlin-type gold deposit, Guizhou, China: implications for gold depositional processes. *Mineral Deposita* 47:653–662
- Su WC, Dong WD, Zhang XC, Shen NP, Hu RZ, Hofstra AH, Cheng LZ, Xia Y, Yang KY (2018) Carlin-type gold deposits in the Dian-Qian-Gui “Golden Triangle” of southwest China. *Rev Econ Geol* 20:157–185
- Suo ST, Hou GJ, Zhang MF, Wang K (1993) The large panjiang river multi-level sheeted thrust-nappe structure in southwestern guizhou. *Regional Geology of China* 3:239–247 (in Chinese with English abstract)
- Suo ST, Bi XM, Zhao WX, Hou GG (1998) Very low-grade metamorphism and its geodynamical signification of Triassic strata within the Youjiang River basin. *Sci Geol Sin* 33:395–405 (in Chinese with English abstract)
- Tan QP, Xia Y, Xie ZJ, Yan J (2015a) Migration paths and precipitation mechanisms of ore-forming fluids at the Shuiyindong Carlin-type gold deposit, Guizhou, China. *Ore Geol Rev* 69:140–156

- Tan QP, Xia Y, Xie ZJ, Yan J, Wei DT (2015b) S, C, O, H, and Pb isotopic studies for the Shuiyindong Carlin-type gold deposit, Southwest Guizhou, China: constraints for ore genesis. *Chin J Geochem* 34(4):525–539
- Tan QP, Xia Y, Wang XQ, Xie ZJ, Wei DT (2017) Carbon-oxygen isotopes and rare earth elements as an exploration vector for Carlin-type gold deposits: a case study of the Shuiyindong gold deposit, Guizhou Province, SW China. *J Asian Earth Sci* 148:1–12
- Tanner D, Henley RW, Mavrogenes JA, Holden P (2016) Sulfur isotope and trace element systematics of zoned pyrite crystals from the El Indio Au–Cu–Ag deposit, Chile. *Contrib Mineral Petrol* 171:33
- Tardani D, Reich M, Deditius AP, Chrystosoulis S, Sánchez-Alfaro P, Wrage J, Roberts MP (2017) Copper–arsenic decoupling in an active geothermal system: a link between pyrite and fluid composition. *Geochim Cosmochim Acta* 204:179–204
- Wang ZS (1997) Affirmation of the Jurassic in Longtoushan of Zhenfeng, Guizhou and its geological significance: Guizhou Geology 14:201–203 (in Chinese with English abstract)
- Wang ZP (2013) Genesis and dynamic mechanism of the epithermal ore deposits, SW Guizhou, China—a case study of gold and antimony deposits. PhD thesis, Institute of Geochemistry, Chinese Academy of Sciences, Guiyang, China, pp 1–162 (in Chinese with English abstract)
- Wang YG, Wang LT, Zhang MF, Wang LL (1995) Texture of the upper crust and pattern of the disseminated gold deposits distributed in Nanpanjiang area. *Guizhou Geology* 12:91–183 (in Chinese with English abstract)
- Wang ZP, Xia Y, Song XY, Yan BW, Tan QP (2013) Sulfur and lead isotopic composition of the Huijiabao Carlin-type gold field and the ore-forming material sources in southwest of Guizhou. *Bull Mineral Petrol Geochem* 32:746–758 (in Chinese with English abstract)
- Wang JL, Lin FC, Yu YS, Wang H, Wu SY (2014) The Indosinian–Yanshanian gold metallogenic system in the Youjiang sedimentary basin, Southwestern China. *Geol Explor* 50:105–113 (in Chinese with English abstract)
- Wu YF, Evans K, Li JW, Fougereuse D, Large RR, Guagliardo P (2019) Metal remobilization and ore-fluid perturbation during episodic replacement of auriferous pyrite from an epizonal orogenic gold deposit. *Geochim Cosmochim Acta* 245:98–117
- Xia Y (2005) Characteristics and model for Shuiyindong gold deposit in southwestern Guizhou, China. PhD Thesis, Institute of Geochemistry, Chinese Academy of Sciences, Guizhou, China, pp 1–123 (in Chinese with English abstract)
- Xiao DC (2012) The study on ore-forming fluids in the Yata Carlin-type gold deposit, Guizhou Province. Master thesis, Chengdu University of Technology, pp 1–63 (in Chinese with English abstract)
- Xie ZJ, Xia Y, Cline JS, Pribil MJ, Koenig A, Tan QP, Wei DT, Wang ZP, Yan J (2018) Magmatic origin for sediment-hosted Au deposits, Guizhou Province, China: In situ chemistry and sulfur isotope composition of pyrites, Shuiyindong and Jinfeng Deposits. *Econ Geol* 113(7):1627–1652
- Yan J, Hu RZ, Liu S, Lin YT, Zhang JC, Fu SL (2018) NanoSIMS element mapping and sulfur isotope analysis of Au-bearing pyrite from Lannigou Carlin-type Au deposit in SW China: new insights into the origin and evolution of Au-bearing fluids. *Ore Geol Rev* 92: 29–41
- Zhang XC (1998) The geology and hydrothermal evolution of sediment-hosted gold deposits in Southwestern Guizhou Province, PRC. Dissertation, Imperial College London (University of London)
- Zhang XJ, Xiao JF (2014) Zircon U–Pb geochronology, Hf isotope and geochemistry study of the Late Permian diabases in the northwest Guangxi autonomous region. *Bull Mineral Petrol Geochem* 33:163–176 (in Chinese with English abstract)
- Zhang XC, Spiro B, Halls C, Stanley CJ, Yang KY (2003) Sediment-hosted disseminated gold Deposits in Southwest Guizhou, PRC: their geological setting and origin in relation to mineralogical, fluid inclusion, and stable-isotope characteristics. *Int Geol Rev* 45:407–470
- Zhang XC, Hofstra AH, Hu RZ, Emsbo P, Su WC, Ridley WI (2005) Geochemistry and $\delta^{34}\text{S}$ of ores and ore stage iron sulfides in Carlin-type gold deposits, Dian-Qian-Gui area, China: implications for ore genesis. *Mineral Deposit Research: Meeting the Global Challenge*. Springer Berlin Heidelberg 1107–1110
- Zhang Y, Xia Y, Wang ZP, Yan BW, Fu ZK, Chen M (2010) REE and stable isotope geochemical characteristics of Bojitian Au deposit, Guizhou Province. *Front Earth Sci* 17:385–395 (in Chinese with English abstract)
- Zhang J, Deng J, Chen HY, Yang LQ, Cooke D, Danyushevsky L, Gong QJ (2014a) LA-ICP-MS trace element analysis of pyrite from the Chang'an gold deposit, Sanjiang region, China: implication for ore-forming process. *Gondwana Res* 26:557–575
- Zhang JC, Lin YT, Yang W, Shen WJ, Hao JL, Hu S, Cao MJ (2014b) Improved precision and spatial resolution of sulfur isotope analysis using NanoSIMS. *J Anal At Spectrom* 29:1934–1943
- Zhao J, Liang JL, Long XP, Li J, Xiang QR, Zhang JC, Hao JL (2018) Genesis and evolution of framboidal pyrite and its implications for the ore-forming process of Carlin-style gold deposits, southwestern China. *Ore Geol Rev* 102:426–436
- Zhu JJ, Hu RZ, Richards JP, Bi XW, Stern R, Lu G (2017) No genetic link between Late Cretaceous felsic dikes and Carlin-type Au deposits in the Youjiang basin, Southwest China. *Ore Geol Rev* 84:328–337
- Zong KQ, Klemm R, Yuan Y, He ZY, Guo JL, Shi XL et al (2017) The assembly of Rodinia: the correlation of early Neoproterozoic (ca. 900 Ma) high-grade metamorphism and continental arc formation in the southern Beishan Orogen, southern Central Asian Orogenic Belt (CAOB). *Precambrian Res* 290:32–48
- Zygouri E, Kiliadis SP, Zack T, Pitcairn I, Fru EC, Nomikou P et al (2017) LA-ICP-MS evidence for Au–Cu coupling in modern sea-floor massive sulphides, Kolombo arc-volcano (Santorini), Greece. *Goldschmidt 2017 Abstract*

Publisher's note Springer Nature remains neutral with regard to jurisdictional claims in published maps and institutional affiliations.